

Characterising the U–Th–Pb systematics of allanite by ID and LA-ICPMS: Implications for geochronology

Andrew J. Smye^{a,*}, Nick M.W. Roberts^a, Daniel J. Condon^a,
Matthew S.A. Horstwood^a, Randall R. Parrish^{a,b}

^aNERC Isotope Geosciences Laboratory, British Geological Survey, Keyworth, Nottingham NG12 5GG, UK

^bDepartment of Geology, University of Leicester, University Road, Leicester LE1 7RH, UK

Received 16 August 2013; accepted in revised form 17 March 2014; available online 26 March 2014

Abstract

Allanite has the potential to be a useful chronometer of crustal evolution, forming in response to a wide spectrum of metamorphic and magmatic conditions and incorporating weight-percent concentrations of LREE, Th and U. Despite its growing use in *in situ* U–Th–Pb geochronology, allanite reference materials lack sufficient U–Th–Pb isotopic characterisation and little is known concerning the response of U–Th–Pb systematics of allanite to hydrothermal alteration and self-irradiation. This contribution presents the results of a combined ID-TIMS and LA-ICPMS U–Th–Pb study on a suite of five allanite crystals, spanning ~2.6 Ga and including three commonly-used allanite reference materials: the Siss, Bona and Tara allanites. Siss and Bona allanites preserve an inherited ca. 1 Ga Pb component, consistent with the presence of xenocrystic allanite cores or the presence of zircon micro-inclusions. Tara allanite yields concordant U–Pb ages (407–430 Ma), but is affected by Th/U fractionation, likely caused by hydrothermal alteration. Additionally, the tendency for Th to become mobilised post-crystallisation is further evidenced by two Precambrian allanite megacrysts, LE40010 (ca. 2.8 Ga) and LE2808 (ca. 1.1 Ga), that both exhibit discordant Th/Pb analyses, linked to the formation of thorite micro-inclusions along hydration pathways. Self-irradiation dose versus discordance relationships show that a percolation threshold is present in allanite at cumulative dose values close to 3×10^{17} α -decay g^{-1} , an order of magnitude smaller than zircon. Collectively, the presence of common-Pb and excess-²⁰⁶Pb, its susceptibility to incur Th/U fractionation and hydrothermal Pb-loss complicates the use of allanite as a geochronometer. These factors explain dispersion of ~4% in the isotopic compositions of Siss and Tara allanites measured by LA-ICPMS, providing a fundamental limit on the accuracy of the allanite chronometer using these reference materials.

© 2014 Elsevier Ltd. All rights reserved.

1. INTRODUCTION

Allanite ($[Ca, REE, Th]_2[Al, Fe^{+3}]_3[SiO_4]_3[OH]$) is an epidote-group mineral that crystallises as an accessory phase in a wide spectrum of metamorphic and magmatic environments. Typical concentrations of Th between 0.05 and 3 wt.% and U between 10 and 3000 ppm (Gieré and

Sorensen, 2004) make allanite a prime target for U–Pb and Th–Pb geochronology. The mineral is integral to the behaviour of geochemically important trace elements, including the rare earth elements (REE), Th, U and Sr. In subducted crust, allanite is the dominant carrier of light rare earth elements (LREE), U and Th, capable of transporting these elements into the mantle (Hermann, 2002; Klimm et al., 2008). In addition to monazite, allanite controls the release and consumption of LREE and Th during regional metamorphism of metasedimentary rocks (Wing et al., 2003). Furthermore, the importance of allanite has long been recognised in the trace element evolution of

* Corresponding author. Current address: Jackson School of Geosciences, University of Texas, Austin, TX 78712, USA. Tel.: +1 512 232 5762.

E-mail address: andrew.smye@jsg.utexas.edu (A.J. Smye).

granitoids, where it crystallizes early during melt differentiation (Miller and Mittlefehldt, 1982; Gromet and Silver, 1983). Its structure is dominated by chains of edge-sharing octahedra, linked by isolated SiO_4 tetrahedra, making it amenable to chemical exchange with clinozoisite ($\text{REE}^{3+} + \text{Fe}^{2+} \leftrightarrow \text{Ca}^{2+} + \text{Al}^{3+}$) and epidote solution end-members ($\text{REE}^{3+} + \text{Fe}^{2+} \leftrightarrow \text{Ca}^{2+} + \text{Fe}^{3+}$; Gieré and Sorensen, 2004). The high degree of chemical flexibility means that allanite has the potential to record trace element signatures that are characteristic of specific metamorphic and magmatic processes. Combined with improved understanding of allanite phase-relations (Janots et al., 2007; Spear, 2010), this geochemical information can be used to form a quantitative linkage between isotopic age and the pressure (P) and temperature (T) conditions of allanite growth (e.g.). Of particular utility to understanding the rates of tectonometamorphic processes is the potential for allanite to provide a high resolution chronology of individual metamorphic reactions, including those occurring during prograde metamorphism (Spandler et al., 2003; Rubatto et al., 2011; Smye et al., 2012), a portion of P – T space that is not accessible by other high- μ ($^{238}\text{U}/^{204}\text{Pb}$) accessory phases such as zircon and rutile.

In igneous systems, allanite typically forms the cores of epidote phenocrysts in metaluminous to felsic melts, pegmatites, dacitic dikes and volcanic tuffs (Kosterin et al., 1961; Dollase, 1971, 1973; Duggan, 1976; Exley, 1980; Gieré, 1986; Chesner and Ettlinger, 1989; Petrik et al., 1995; Broska et al., 2000; Gieré and Sorensen, 2004; Beard et al., 2006; Cox et al., 2012). Often, it is noted that the total REE and Th content decreases from core to rim, accompanied by an increase in the concentration of Fe^{3+} (Gieré and Sorensen, 2004). Collectively, these chemical relationships in igneous allanite have been interpreted to suggest that crystallization of allanite–epidote–clinozoisite solid solutions in silicic melts is controlled by the concentrations of REE and Th (Gromet and Silver, 1983). Metamorphic allanite is primarily found in metapelitic rocks (Smith and Barreiro, 1990; Wing et al., 2003), but is also present in mafic eclogites (Hermann, 2002; Parrish et al., 2006), metacarbonates (Boundy et al., 2002) and granitic gneisses (Finger et al., 1998). A number of studies have examined progressive metamorphic sequences to constrain accessory phase relationships (Smith and Barreiro, 1990; Kingsbury et al., 1993; Wing et al., 2003; Kohn and Malloy, 2004; Fitzsimons et al., 2005; Janots et al., 2006, 2008; Rasmussen et al., 2006; Tomkins and Pattison, 2007). Despite differences in the relative appearance of allanite and monazite, these investigations highlight the importance of bulk-rock CaO and LREE content in stabilising allanite over monazite. In rocks of sufficient CaO and LREE, allanite forms at the expense of metamorphic or detrital monazite under low-temperature (350–450 °C) conditions (Wing et al., 2003; Janots et al., 2008, 2009) and breaks down at conditions close to the staurolite isograd (Janots et al., 2008, 2009). However, given the complex nature of allanite chemistry, further investigation is required to fully resolve the relationship between allanite stability and bulk rock composition (Spear, 2010). Allanite can also form along low geothermal gradients, during the prograde stages of

(ultra-) high pressure metamorphism. Specifically, Smye et al. (2012) showed that metamorphic allanite grew prior to garnet growth during prograde Alpine subduction and retained its radiogenic Pb to temperatures in excess of 600 °C. Accordingly, allanite geochronology offers a method to constrain rates of prograde heating and implied burial during orogenesis (Janots et al., 2009).

Despite its common occurrence in a wide range of lithologies, allanite has received relatively little attention as a geochronometer compared to other common accessory minerals such as zircon, rutile and monazite. Largely, this is because U–Th–Pb allanite geochronology is hampered by: (i) the propensity of allanite to sequester high levels of non-radiogenic Pb and the related uncertainty arising from its correction (e.g. Gabudianu Radulescu et al., 2009); (ii) the presence of excess- ^{206}Pb , arising from incorporation of ^{230}Th (Oberli et al., 2004); (iii) its common lack of crystallographic integrity and its susceptibility to metasomatic alteration (Poitrasson, 2002), and (iv) its tendency to incorporate radiogenic Pb from precursor phases (Romer and Siegesmund, 2003). Given that allanite is commonly zoned, previous studies have focused on developing specific methodologies for *in situ* dating of allanite by SHRIMP (Catlos et al., 2000; Gregory et al., 2007) and LA-ICPMS (Gregory et al., 2007; Darling et al., 2012a). Unlike isotope dilution (ID) methods, which do not require normalisation to minerals of ‘known age’ (Heaman and Parrish, 1991; Hodges et al., 1996), microbeam (SIMS and LA-ICPMS) methods require analyses of unknowns relative to a reference mineral of known composition and age. The accuracy of these *in situ* methods for extracting chronometric information from allanite is limited by the U–Th–Pb isotopic characterisation of the reference material. Currently, allanite reference materials are poorly characterised and often the age/isotopic composition of the material relies upon assumed concordance between U–Pb and Th–Pb systems, the use of multigrain-fraction ID analyses and/or assumed concordance with cogenetic zircon ages. There is a notable dearth of accurate U–Pb, and particularly, Th–Pb ID data for commonly used allanite reference materials.

To address this shortfall, we present the results of a combined ID-TIMS and LA-ICPMS U–Th–Pb isotopic study on a suite of five allanite samples ranging from ~30 Ma to ~2.7 Ga, including the Siss, Bona and Tara allanite standards currently in use as reference materials for *in situ* allanite geochronology (Gregory et al., 2007; Darling et al., 2012). We also characterise two previously undated Precambrian allanite megacrysts, LE40010 and LE2808, to investigate the physiochemical mechanisms responsible for U–Th–Pb discordance in allanite. Both LA-ICPMS and ID analyses have been performed on the *same* allanite grain fractions, permitting rigorous assessment of allanite U–Th–Pb isotope systematics and the physical mechanisms responsible for limiting the final age uncertainties. As the application of allanite U–Th–Pb geochronology to studies of crustal evolution becomes more widespread (e.g. Cenki-Tok et al., 2011; Rubatto et al., 2011; Manzotti et al., 2012), it is vitally important to understand the limitations and strengths of allanite as a geochronometer.

2. ALLANITE SAMPLES

2.1. LE40010

Allanite LE40010 is a quartz pegmatite-hosted megacryst (~2 cm length; ~1 cm width) collected by B. F. Windley in 1950 from the late-Archaean Fiskenaesset anorthosite complex, western Greenland and made available by the University of Leicester. Individual shards of allanite measuring 400–600 μm were separated from the megacryst for use in this study. Allanite LE40010 is dark-brown, vitreous and displays conchoidal fractures. Backscattered electron imaging (Fig. 2a) shows that fragments are characterised by an increase in clinozoisite content towards grain edges; domains of unzoned allanite contain ~0.7 cations per formula unit (c.p.f.u.) REE and 2–2.5 wt.% ThO_2 (Figs. 1 and 2a; Table S1). Small (<10 μm diameter) quartz inclusions are abundant throughout. Fragments also show varying degrees of post-crystallisation hydrothermal alteration, including cracks that are concentrated in regions <200 μm diameter and contain rounded to elongate inclusions of thorite (>85 wt.% ThO_2) and uraninite (>98 wt.% UO_2), typically <20 μm in diameter. The high actinide concentrations and Archean age of this allanite means that this sample offers an opportunity to study the effect of large cumulative self-irradiation dose on U–Th–Pb systematics.

2.2. LE2808

Allanite LE2808 is another pegmatite-hosted megacryst (~1 cm length; ~0.7 cm width) sourced from the University of Leicester mineral collection. Details concerning the sample's geological context are absent. The megacryst is dark-brown–black and displays an intense vitreous lustre. Individual shards <400 μm diameter were separated from the megacryst for isotopic analysis. Backscattered electron imaging shows that unaltered portions of the megacryst are compositionally homogeneous, containing ~0.8 c.p.f.u. REE and 1.3–1.7 wt.% ThO_2 (Figs. 1 and 2b;

Table S1). Evidence for hydrothermal alteration is restricted to small (<50 μm) domains of LREE depleted allanite ($\Sigma\text{REE} = 0.7$ c.p.f.u.) adjacent to cracks that also contain rare inclusions of thorite (<5 μm diameter; >51 wt.% ThO_2).

2.3. Siss and Bona

The Siss and Bona allanites originate from a weakly-foliated tonalite and a granodiorite, respectively, both of which pertain to the Central-Alpine Bergell intrusion. The grains used in this study were taken from the bulk-rock samples used by von Blanckenburg (1992), who used ID-TIMS to measure $^{208}\text{Pb}/^{232}\text{Th}$ ages of 31.5 ± 0.4 Ma from eleven single crystals of Siss allanite and 30.1 ± 0.1 Ma from five grains of Bona allanite. Siss allanite grains are <300 μm diameter, anhedral and overgrown by sub-solidus epidote rims. Backscattered electron images (Fig. 2c) reveal diffuse heterogeneity in core regions that corresponds to zoning in REE, Fe and actinide concentrations; light zones contain ~0.5 c.p.f.u. REE + Th, relative to <0.45 c.p.f.u. in darker zones (Figs. 1 and 2c; Table S1). Furthermore, BSE imaging fails to reveal the presence of any obvious included phases. Bona allanite grains are larger (<400 μm diameter) and more homogenous than Siss allanite (Fig. 2d), forming vitreous, euhedral lozenges with thin epidote rims. Bona is enriched in REE and Th, relative to Siss allanite, containing 0.6–0.7 c.p.f.u. REE + Th (Figs. 1 and 2d; Table S1). Both allanite fractions are interpreted to have crystallised early within the history of the melt-evolution of the Bergell pluton at temperatures between 700 and 800 $^\circ\text{C}$, typical of the liquidus interval (von Blanckenburg, 1992; Oberli et al., 2004).

2.4. Tara

The Tara allanite originates from a granodiorite member of the Berridale Batholith, southeast Australia and is described by Gregory et al. (2007). Tara zircons crystallised

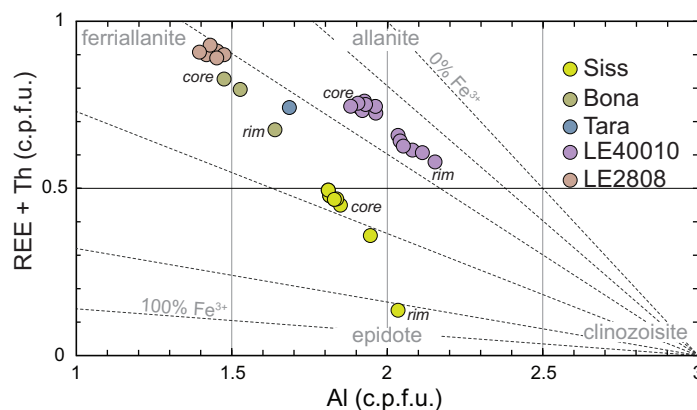


Fig. 1. Allanite compositions determined by EPMA and EDS + WDS SEM analysis. REE + Th versus Al (cations per formula unit) plot after Petrik et al. (1995) and Gieré and Sorensen (2004). The diagram shows representative chemical analyses from each of the allanite samples considered in this study and their chemical position in the allanite–ferriallanite–epidote–clinozoisite solid solution series. Grey lines radiating from the clinozoisite endmember represent lines of constant Fe-oxidation state and are labelled as a percentage of $\text{Fe}^{3+}/\text{Fe}_{\text{total}}$. Chemical data are presented in Table S1; Tara composition is from Gregory et al. (2007).

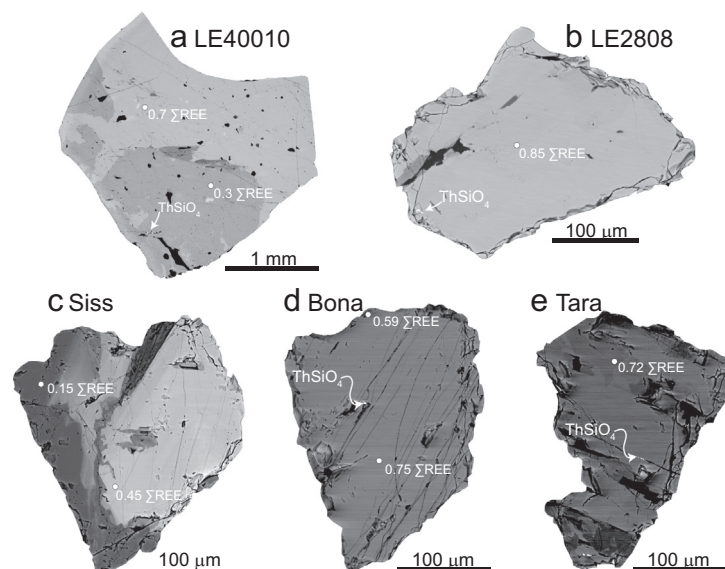


Fig. 2. Backscattered electron images of allanite samples. (a) LE40010; (b) LE2808; (c) Siss; (d) Bona; (e) Tara. Σ REE values in c.p.f.u. are taken from WDS SEM and EPMA analyses. Note the presence of secondary thorite adjacent to cracks.

by 418.7 ± 4.2 Ma as determined by U–Pb SHRIMP analyses (Ickert and Williams, 2011); biotite–feldspar–whole-rock Rb–Sr, biotite K–Ar and ^{40}Ar – ^{39}Ar geochronology yield slightly younger ages, consistent with cooling by 412 ± 1.4 Ma (Williams et al., 1982). Allanite grains are <400 μm diameter, anhedral and exhibit a vitreous lustre. Backscattered electron images (Fig. 2e) reveal subtle gradients in atomic number, consistent with electron probe data from Gregory et al. (2007), showing <1 wt.% difference in Ce_2O_3 across single allanite grains. Grains are crosscut by cracks that host small (<5 μm) aggregates of Ce_2O_3 , representing minor post-crystallisation alteration. Rare inclusions of thorite <1 μm diameter, containing ~ 20 wt.% ThO_2 , are present within the grain matrix. Prior to this study no published ID-TIMS U–Th–Pb data existed for Tara allanite.

3. ANALYTICAL TECHNIQUES

3.1. Isotope dilution

Isotope Dilution (ID) analyses were performed at the NERC Isotope Geosciences Laboratories (NIGL). Target allanite grains (<300 μm diameter) were washed in 2% HNO_3 , reagent-grade organic solvents (acetone and ethanol) and milli-Q™ H_2O in an ultrasonic bath to remove surface contamination prior to loading into Savillex Teflon® microcapsules and addition of a mixed ^{233}U – ^{235}U – ^{230}Th – ^{205}Pb tracer, prepared in 1995 by Parrish at the Geological Survey of Canada. Allanite shards were dissolved in a 50:50 mix of 29 N HF: 16 N HNO_3 ; microcapsules were housed in 125 ml Parr-style bombs and kept at 220 °C for 60+ hours. Total dissolution of samples was verified by visual inspection of vessels containing larger fragments in a given batch. Following dissolution, samples were dried to fluorides then re-dissolved in 11 N HCl at 180 °C, over ~ 12 h. Uranium and Pb were separated using

U-TEVA and AG-1 cation exchange resins, respectively, on standard-size columns (10 mm diameter). Thorium was separated from collected washes using TRUSPEC resin and larger columns (12 mm diameter). U–Pb measurements were performed at NIGL using standard protocols (e.g. Smye et al., 2012). Thorium was analysed in a 2% HNO_3 solution on a Nu Plasma MC-ICPMS. Mass-dependent Th fractionation was measured by repeated analysis of a 10 ppb ^{230}Th – ^{232}Th solution obtained in 1995 by Parrish from the Geological Survey of Canada and measured by TIMS in Ottawa using single and double filament methods, and MC-ICPMS ($^{230}\text{Th}/^{232}\text{Th} = 7.0724 \pm 0.007$, 1σ) using U500 equal atom for normalisation on a VG P54 instrument in 1997. Both ^{230}Th and ^{232}Th were measured on Faraday collectors (H1 and H3, respectively). Reported isotope ratios, which are averages of 30 individual analyses (1 block), were calculated using an in-house Excel spreadsheet. U–Th–Pb ratios and uncertainties (corrected for fractionation, laboratory blank and tracer) were calculated using the algorithms of Schmitz and Schoene (2007). Ages were calculated using Isoplot v.3 (Ludwig, 2003a).

3.2. LA-ICPMS

Allanite shards were picked under reflected light using a binocular microscope; grains were then mounted in epoxy resin for *in situ* analysis and grain mounts were washed in 2% HNO_3 and milli-Q™ water to minimise potential surface contamination, such as common-Pb. Uranium, Th and Pb isotope data were collected using a New Wave Research UP193SS Laser Ablation system coupled to a Nu Instruments AttoM single-collector sector-field inductively coupled plasma mass spectrometer (SC-ICPMS). A large-format New Wave Research cell was used—a two-volume design featuring a moveable cup that decreases the ablation volume and washout time to <0.5 s. Optimal

signal strengths were attained using the following ablation parameters: 35 μm spot diameter; 5 Hz; 1.9–2.5 J/cm²; 10 s wait between ablations to ensure sample washout and a 30 s ablation time. Oxide production was minimised by tuning the gas flows such that ThO <0.4%, and UO <0.1%. Before each analysis, the grain surface was cleaned by rastering the laser beam over the target area ($\sim 700 \mu\text{m}^2$), at a low fluence. The energy profile of the beam was stabilised by firing the laser for 10 s behind the shutter prior to each ablation. On ablation, sample aerosols were transported using a He carrier gas; Ar was introduced into the sample line via a T-piece midway between the cell and torch to form a $\sim 50:50$ Ar–He mix. The detection system in the NIGL Nu AttoM comprises a single MasCom secondary electron multiplier. The AttoM was operated in peak-jumping mode which permits measurement of ²⁰²Hg, ²⁰⁴Pb + Hg, ²⁰⁶Pb, ²⁰⁷Pb, ²⁰⁸Pb, ²³²Th, and ²³⁵U during a single scan of the electrostatic analyser, whilst the magnet current is held static. Each data integration records 100 sweeps of the measured masses, which roughly equates to 0.18 s. On-mass dwell times are 400 μs on ²⁰⁷Pb and ²³⁵U, and 200 μs on all other masses; switching between masses takes 40 μs . Since ²⁰⁸Pb and ²³²Th are large signals relative to other masses in allanites, these masses use the attenuation mechanism on the Nu AttoM, which reduces the signal intensity by a factor of ~ 350 . ²³⁸U is calculated from the measured ²³⁵U $\times 137.88$ (Note, because the ²³⁸U/²³⁵U value for these allanites has not been determined and [Hiess et al. \(2012\)](#) demonstrated significant variability in the U isotopic composition of non-zircon accessory phases, we use the older, lower precision value compared to the zircon value of [Hiess et al. \(2012\)](#)).

Mass bias fractionation is inherent to ICPMS and likely originates from mass- and charge-dependent processes operating during sample ablation and introduction of sample aerosol into the plasma (e.g. [Tanner et al., 1994](#)). Correction for instrumental drift and laser-induced elemental fractionation was addressed via analysis of zircon standard–91500 ([Wiedenbeck et al., 1995](#)) and allanite LE40010 (*this study*), using a standard-sample-bracketing routine. Reduction of isotopic data was performed off-line using an in-house Excel spreadsheet. Ages were calculated at the 95% confidence level using Isoplot v.3 ([Ludwig, 2003b](#)) and the decay constant recommended by the IUGS Subcommittee in Geochronology ([Steiger and Jäger, 1977](#)).

3.3. Scanning electron microscopy and chemical analysis

Allanite grains were imaged using the British Geological Survey's LEO (Zeiss) 435VP Variable Pressure Digital Scanning Electron Microscope (SEM) operated in backscatter detection mode (20 kV accelerating voltage, 3.6–3.7 nA beam current at 15 mm working distance). Backscatter images reflect variations in the relative concentrations of high-atomic number elements (REEs + U and Th) between individual micro-domains. Quantitative characterisation of the allanite samples was undertaken using an Energy Dispersive System (EDS; Oxford Instruments INCA Energy 450 System); U, Th, Sm and Gd

were measured using a Wavelength Dispersive System (WDS; Oxford Instruments INCA Wave 700 Series). Analyses were calibrated to a pure Co reference material. On-peak counting times varied between 20 and 30 s. Dead time (30–40%) and background electron emission were corrected for using an online ZAF procedure. Quantitative allanite analyses were normalised to 8 cations and 12.5 oxygens; $\text{Fe}^{3+}/\text{Fe}^{2+}$ was calculated using the charge-balance criteria: $\sum(\text{Si} + \text{Al} + \text{Fe} + \text{Ti} + \text{Mn} + \text{Mg}) = 6$ c.p.f.u. ([Ercit, 2002](#)). Additional quantitative analyses were performed using a Cameca SX-100 electron microprobe at the University of Cambridge. Major element analyses were acquired using a 15 keV accelerating voltage, a beam current of 10 nA and 20 s data collection time. REE and trace element acquisition used 15 keV, 200 nA and 100 s, respectively. Natural and synthetic minerals and oxides were used as standards. Raw data were corrected on-line according to Cameca X-PHI procedure.

3.4. X-ray diffraction

Allanite samples were ground to a fine powder (~ 0.1 g) and mounted on glass slides in ethanol. Measurements were performed on a Bruker D8 diffractometer at the University of Cambridge, using Cu K $_{\alpha 1}$ radiation; samples slides were loaded into an automatic sample changer and diffraction patterns spanning 10–100° 2 θ were acquired with a spacing of 0.02° 2 θ and 2 s dwell time. The metamict nature of the diffraction patterns obtained from allanite samples LE40010 and LE2808 precluded lattice parameter refinement.

4. RESULTS

The U–Th–Pb ID and LA-ICP-MS data are presented in [Tables 1](#) and [S2](#), respectively. LA-ICP-MS and U–Pb ID-TIMS data were collected over three analytical sessions between January and April 2012. Th ID measurements were carried out over 3 analytical sessions between October 2011 and March 2012. The salient features of each U–Th–Pb data set are summarised beneath.

4.1. LE40010

U–Pb ID-TIMS isotopic analysis was performed on 16 fractions separated from a single megacryst; all grains were dark brown, vitreous and measured <100 μm diameter. Th isotopes were measured on 12 of these fractions. Values of Th/U vary between 130 and 223, and Pb is dominantly radiogenic ($\text{Pb}^*/\text{Pb}_c = 72\text{--}359$; $^{206}\text{Pb}/^{204}\text{Pb} = 87\text{--}445$). Uncorrected U–Pb analyses show considerable scatter in Tera–Wasserburg space, precluding accurate determination of a lower intercept age ([Fig. 3a](#)). Corrected U–Th–Pb ID analyses (2.8 Ga; [Stacey and Kramers, 1975](#)) are strongly discordant ([Fig. 3b](#) and [c](#)). Plotted in Wetherill Concordia coordinate space, grain fractions a1, c4 and j3 form a discordia, consistent with recent Pb-loss, whereas the remaining grain fractions form a sub-concordant array between 2600 and 2750 Ma ([Fig. 3b](#)); two grain fractions,

Table 1
Allanite ID U–Th–Pb isotopic data.

Fractions ^a	Compositional parameters			Radiogenic isotope ratios								Sample (radiogenic + initial Pb) isotope ratios															
	Th/ U ^b	Pb ^a / Pb _c ^c	Pb _c ^c (pg)	²⁰⁶ Pb/ ²⁰⁴ Pb ^d	²⁰⁸ Pb/ ²⁰⁶ Pb ^e	²⁰⁷ Pb/ ²⁰⁶ Pb ^e	% err ^f	²⁰⁷ Pb/ ²³⁵ U ^e	% err ^f	²⁰⁶ Pb/ ²³⁸ U ^e	% err ^f	ρ _{7/5} -6/8 ^g	²⁰⁸ Pb/ ²³² Th ^e	% err ^f	²³⁸ U/ ²⁰⁶ Pb ^h	% err ^f	²⁰⁷ Pb/ ²⁰⁶ Pb ^h	% err ^f	ρ _{38/6} -7/6 ^g	²⁰⁴ Pb/ ²⁰⁶ Pb ^h	% err ^f	²⁰⁸ Pb/ ²⁰⁴ Pb ^h	% err ^f	²⁰⁸ Pb/ ²³² Th ^h	% err ^f		
<i>LE40010</i>																											
Allanite a1	216	349.24	45	358.01	62.624	0.18508	0.15	12.292	0.23	0.4817	0.12	0.80	0.14375	2.02	2.000	0.14	0.2178	0.30	-0.83	0.00269	1.90	22446.3	2.01	0.14501	2.07		
Allanite a2	211	408.52	18	445.82	58.902	0.18492	0.14	13.090	0.26	0.5134	0.17	0.87	0.14352	2.10	1.894	0.25	0.2097	0.62	-0.82	0.00204	5.13	28167.3	5.33	0.14473	5.35		
Allanite a3	211	218.80	61	255.23	55.708	0.18159	0.19	13.921	0.29	0.5560	0.18	0.75	0.13943	2.21	1.705	0.18	0.2282	0.30	-0.67	0.00382	1.37	13873.9	1.49	0.14078	1.62		
Allanite a4	207	216.62	14	247.39	58.091	0.18481	0.19	12.914	0.31	0.5068	0.19	0.80	0.14355	1.91	1.877	0.48	0.2283	1.29	-0.98	0.00357	6.66	15507.0	7.13	0.14490	7.15		
Allanite c1	160	82.66	53	126.58	44.874	0.17367	0.34	11.670	0.39	0.4874	0.24	0.50	-	-	1.837	0.27	0.2683	0.53	-0.94	0.00768	1.46	5265.8	1.71	-	-		
Allanite c2	203	306.12	23	352.03	56.109	0.18507	0.17	13.309	0.25	0.5216	0.14	0.78	0.01419	1.82	1.848	0.22	0.2172	0.58	-0.91	0.00264	3.83	20523.6	4.03	0.01432	4.06		
Allanite c3	201	275.84	25	322.11	55.400	0.18478	0.16	13.323	0.24	0.5229	0.13	0.80	0.02540	1.84	1.837	0.22	0.2201	0.58	-0.95	0.00290	3.51	18368.2	3.71	0.02563	3.75		
Allanite c4	196	142.82	29	144.03	68.083	0.18595	0.34	9.203	0.43	0.3589	0.27	0.63	0.02281	1.87	2.536	0.42	0.2660	0.85	-0.92	0.00658	2.77	9447.5	3.17	0.02306	3.24		
Allanite d1	178	257.25	255	333.18	49.180	0.18428	0.16	13.211	0.24	0.5199	0.13	0.78	0.63861	1.92	1.845	0.11	0.2206	0.10	-0.69	0.00298	0.36	15853.5	0.43	0.64460	0.67		
Allanite d2	189	230.12	198	277.78	53.337	0.18357	0.18	12.731	0.24	0.5030	0.12	0.71	0.38672	2.38	1.891	0.09	0.2271	0.11	-0.84	0.00357	0.44	14243.1	0.51	0.39044	0.76		
Allanite d3	130	157.71	171	279.16	36.004	0.18051	0.18	12.788	0.29	0.5138	0.19	0.79	0.69110	1.90	1.852	0.17	0.2239	0.12	-0.45	0.00355	0.51	9688.4	0.61	0.69852	0.83		
Allanite d4	131	153.24	99	264.97	37.044	0.17959	0.19	12.260	0.31	0.4951	0.22	0.80	0.27938	3.10	1.917	0.21	0.2250	0.19	-0.42	0.00371	0.86	9505.1	0.95	0.28240	1.11		
Allanite d5	147	74.89	221	125.78	40.618	0.18079	0.34	12.847	0.38	0.5154	0.23	0.46	0.42072	2.07	1.731	0.12	0.2773	0.14	-0.74	0.00790	0.38	4622.4	0.49	0.42685	1.24		
Allanite j1	224	72.77	32	87.48	61.170	0.18591	0.48	13.606	0.55	0.5308	0.39	0.54	-	-	1.603	0.61	0.3189	0.98	-0.96	0.01094	2.29	4792.2	2.88	-	-		
Allanite j2	188	300.15	12	372.84	52.426	0.18357	0.26	12.908	0.37	0.5100	0.23	0.72	-	-	1.899	0.41	0.2117	1.11	-0.90	0.00231	8.21	22048.2	8.58	-	-		
Allanite j3	179	240.41	5	293.09	56.516	0.18480	0.37	10.683	0.61	0.4193	0.41	0.81	-	-	2.316	1.28	0.2107	3.86	-0.99	0.00213	30.85	25786.3	32.11	-	-		
Allanite j4	190	277.27	11	344.60	52.727	0.18542	0.27	13.251	0.38	0.5183	0.22	0.73	-	-	1.865	0.47	0.2152	1.32	-0.94	0.00245	9.29	20817.5	9.73	-	-		
<i>LE2808</i>																											
Allanite 1	48	73.75	868	347.79	14.494	0.075	0.27	1.893	0.40	0.1826	0.25	0.75	-	-	5.211	0.24	0.1160	0.10	-0.28	0.00287	0.23	4847.8	0.26	-	-		
Allanite 2	43	61.09	1175	312.52	13.359	0.075	0.60	1.746	0.69	0.1677	0.34	0.51	0.12428	0.34	5.639	0.30	0.1209	0.15	-0.15	0.00319	0.36	3995.0	0.22	0.05586	0.33		
Allanite 3	47	85.06	711	405.16	14.229	0.075	0.24	1.894	0.31	0.1826	0.12	0.72	0.03163	0.54	5.250	0.10	0.1102	0.10	-0.68	0.00246	0.26	5582.8	0.17	0.01226	0.43		
Allanite 4	46	90.06	2727	443.48	13.671	0.075	0.23	1.943	0.31	0.1873	0.15	0.74	0.22692	0.33	5.134	0.13	0.1073	0.10	-0.52	0.00225	0.17	5873.9	0.15	0.08925	0.32		
Allanite 5	52	38.21	26	175.73	15.837	0.074	0.55	1.833	1.02	0.1786	0.83	0.84	0.00028	0.72	5.116	1.01	0.1472	2.88	-0.60	0.00511	5.75	2867.3	3.18	0.00010	0.71		
Allanite 6	43	30.24	5	172.21	12.990	0.076	0.98	1.949	1.31	0.1851	0.54	0.74	-	-	5.175	3.46	0.1118	22.77	-0.99	0.00250	70.89	5020.7	37.40	-	-		
Allanite 7	49	45.12	64	218.10	14.627	0.075	0.40	1.943	0.47	0.1874	0.17	0.54	-	-	4.940	0.22	0.1377	0.99	-0.91	0.00440	2.16	3116.0	1.18	-	-		
Allanite 8	47	74.08	69	350.90	14.449	0.075	0.30	1.852	1.18	0.1786	1.12	0.97	-	-	5.341	1.13	0.1142	0.72	-0.10	0.00274	2.07	5070.1	1.09	-	-		
<i>SISS</i>																											
Allanite 1	90	0.68	64	19.95	41.277	0.06748	66.04	0.049	63.75	0.0052	24.64	0.10	0.00150	1.85	11.764	1.52	0.7883	0.16	-0.81	0.05001	0.23	89.6	0.29	0.00267	1.82		
Allanite 2	36	0.56	47	21.60	13.558	0.05477	34.03	0.035	33.62	0.0047	10.20	0.11	0.00147	1.86	29.144	1.94	0.7287	0.35	-0.96	0.04600	0.40	79.2	0.30	0.00291	1.82		
Allanite 3	32	0.36	143	20.06	19.522	0.09019	46.72	0.056	42.73	0.0045	23.01	0.09	0.00142	1.89	14.602	0.67	0.7868	0.10	-0.62	0.04980	0.18	64.5	0.30	0.00361	1.82		
Allanite 4	6	0.46	26	30.05	1.950	0.04641	9.86	0.034	9.87	0.0054	2.49	0.13	0.00152	1.90	73.739	2.53	0.5237	1.60	-1.00	0.03223	1.72	62.8	0.33	0.00401	1.82		
Allanite 5	72	0.51	44	19.92	31.501	0.06383	75.76	0.032	74.84	0.0036	24.83	0.13	0.00147	1.88	17.076	2.25	0.7882	0.21	-0.86	0.05002	0.31	77.4	0.32	0.00296	1.82		
Allanite 6	1	0.19	61	28.34	0.377	0.07113	7.63	0.410	7.32	0.0418	3.06	0.11	0.00225	3.66	8.261	1.12	0.5712	0.56	-0.99	0.03486	0.64	42.6	0.33	0.02585	1.82		
Allanite 7	125	2.17	18	22.90	37.427	0.04390	28.77	0.045	28.87	0.0075	6.53	0.13	0.00153	1.83	26.639	5.05	0.6771	1.33	-0.99	0.04263	1.38	214.5	0.27	0.00188	1.82		
Allanite 8	12	1.25	102	33.71	5.149	0.06622	5.33	0.190	5.18	0.0208	1.99	0.12	0.00154	1.83	21.600	0.56	0.4906	0.42	-0.99	0.02940	0.49	117.4	0.27	0.00233	1.82		
Allanite 9	28	1.39	170	26.70	11.931	0.06360	10.37	0.080	10.06	0.0091	3.77	0.10	0.00150	1.84	32.822	0.43	0.6041	0.19	-0.95	0.03732	0.26	134.7	0.28	0.00213	1.82		
<i>Bona</i>																											
Allanite 1	92	0.68	153	20.36	31.399	0.04968	67.71	0.039	66.88	0.0057	19.16	0.10	-	-	13.708	0.62	0.7730	0.12	-0.57	0.04904	0.18	-	-	-	-		
Allanite 2	154	1.66	70	21.75	40.575	0.03830	44.07	0.034	43.88	0.0064	10.00	0.10	-	-	21.819	1.27	0.7232	0.26	-0.87	0.04578	0.30	-	-	-	-		
Allanite 3	156	0.89	73	20.87	30.881	0.02854	86.84	0.014	87.16	0.0035	14.24	0.10	-	-	29.525	1.29	0.7518	0.22	-0.75	0.04775	0.30	-	-	-	-		
Allanite 4	36	1.24	114	22.66	22.684	0.09420	22.46	0.122	22.98	0.0094	7.98	0.24	-	-	18.381	0.81	0.7060	0.32	-0.43	0.04398	0.45	-	-	-	-		
<i>Tara</i>																											
Allanite 4	129	13.09	12	41.57	39.362	0.05364	8.72	0.511	9.18	0.0691	1.33	0.41	0.01643	1.91	8.828	4.09	0.3696	5.36	-1.00	0.02161	6.15	1149.5	0.44	0.01711	3.59		

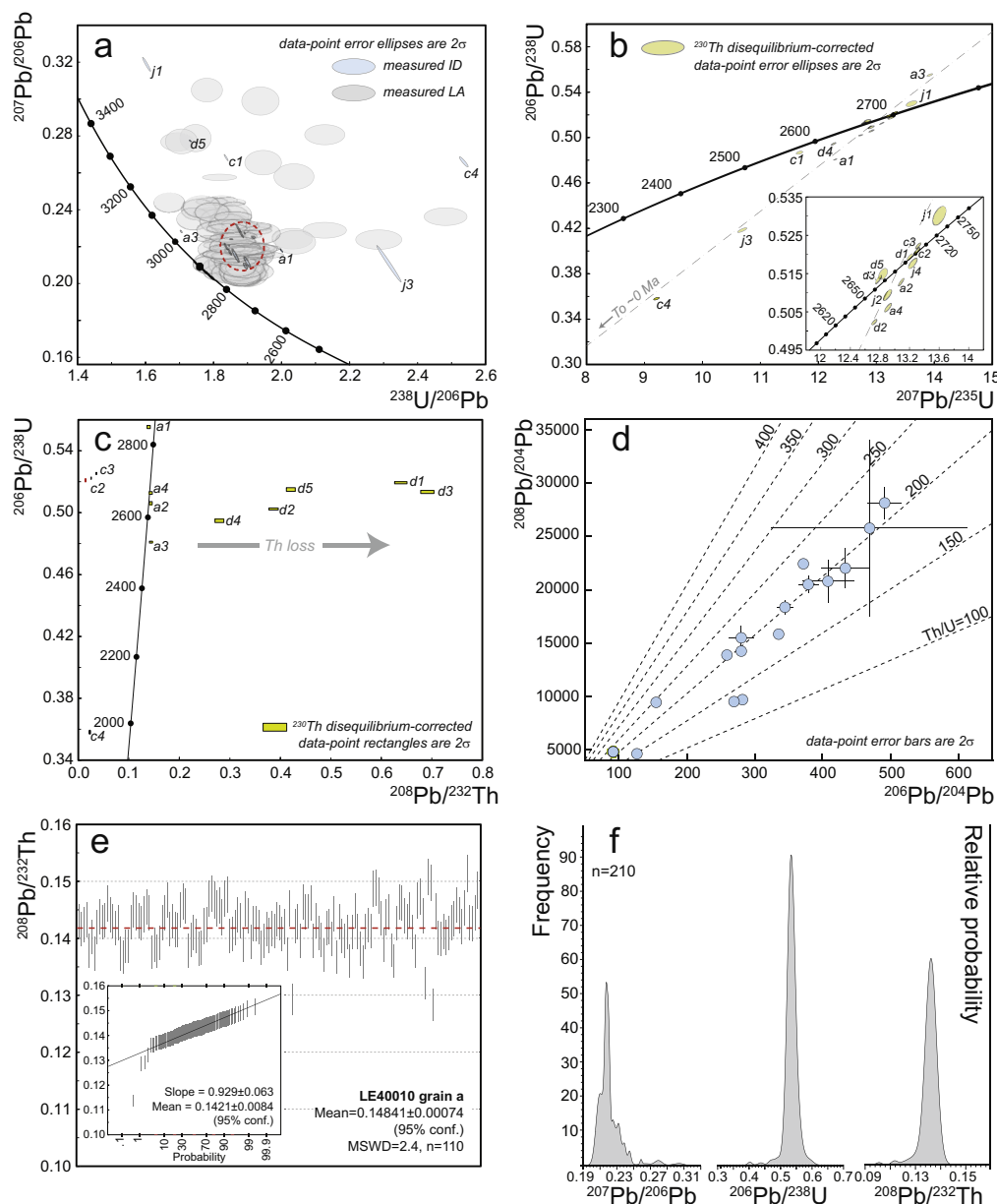


Fig. 3. U–Th–Pb ID and LA-ICPMS results for allanite sample LE40010. (a) Tera–Wasserburg concordia showing raw LA (grey ellipses) and ID analyses (blue ellipses) measured on the same grain fractions. LA analyses are normalised to the average $^{207}\text{Pb}/^{206}\text{Pb}$ and $^{238}\text{U}/^{206}\text{Pb}$ values of the ten ID analyses that form a discrete cluster (red dashed-line). Concordia ages are in Ma and small italicised labels correspond to ID grain fraction notations. (b) Wetherill concordia for ID analyses corrected for common-Pb using a model 2.7 Ga terrestrial Pb composition (Stacey and Kramers, 1975), and excess- ^{206}Pb using a $\text{Th}/\text{U}_{\text{whole-rock}}$ value of 5. (c) $^{206}\text{Pb}/^{238}\text{U}$ – $^{208}\text{Pb}/^{232}\text{Th}$ concordia diagram showing evidence for extreme Th/U fractionation. (d) Pb evolution diagram contoured with 2.7 Ga isochrons for values of allanite Th/U between 100 and 400. Isochrons were calculated using an initial $^{208}\text{Pb}/^{204}\text{Pb} = 33.37$ and $^{206}\text{Pb}/^{204}\text{Pb} = 13.64$. (e) Weighted average of $^{208}\text{Pb}/^{232}\text{Th}$ single-spot LA-ICPMS measurements of LE40010 grain a, collected over three separate analytical sessions. Ratios are normalised to an average of four ID analyses performed on fragments of the same grain. Inset, linearised probability plot of grain a data points. (f) Probability density plots of $^{207}\text{Pb}/^{206}\text{Pb}$, $^{206}\text{Pb}/^{238}\text{U}$ and $^{208}\text{Pb}/^{232}\text{Th}$ ratios collected by LA-ICPMS from four grain fragments, across three analytical sessions ($n = 210$); data are not corrected for common-Pb. (For interpretation of the references to colour in this figure legend, the reader is referred to the web version of this article.)

discordant suggesting post-crystallisation Pb-loss, whereas grain 7 is reversely discordant. Allanite LE2808 exhibits extreme discordance between corrected ID $^{208}\text{Pb}/^{232}\text{Th}$ and $^{206}\text{Pb}/^{238}\text{U}$ analyses (Fig. 5c). The four shards analysed for Th isotopic composition yield apparent $^{208}\text{Pb}/^{232}\text{Th}$ ages between 5 and 4133 Ma. Such dispersion in

$^{208}\text{Pb}/^{232}\text{Th}$ ratios is notably similar to the Th–Pb data produced from allanite LE40010 and reflects fractionation of ^{232}Th from ^{208}Pb over length scales in excess of the digested grain diameter ($\sim 400\ \mu\text{m}$). The Pb composition of analysed grain fragments suggests that effective Th/U ratios varied between 40 and 55 (Fig. 5d). Given the dispersion in

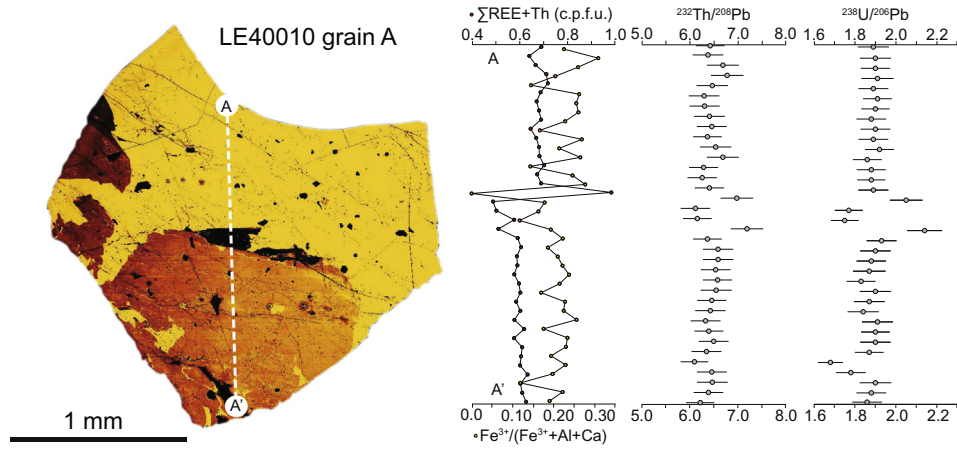


Fig. 4. Chemical and U–Th–Pb isotopic profile across allanite LE40010 grain A (Fig. 2a). Grain image uses a false-colour BSE display to highlight regions of unaltered (yellow) and altered allanite (black to dark orange). Note the relationship between Ca (+Al) content of the allanite and the degree of U–Th–Pb isotopic disturbance. (For interpretation of the references to colour in this figure legend, the reader is referred to the web version of this article.)

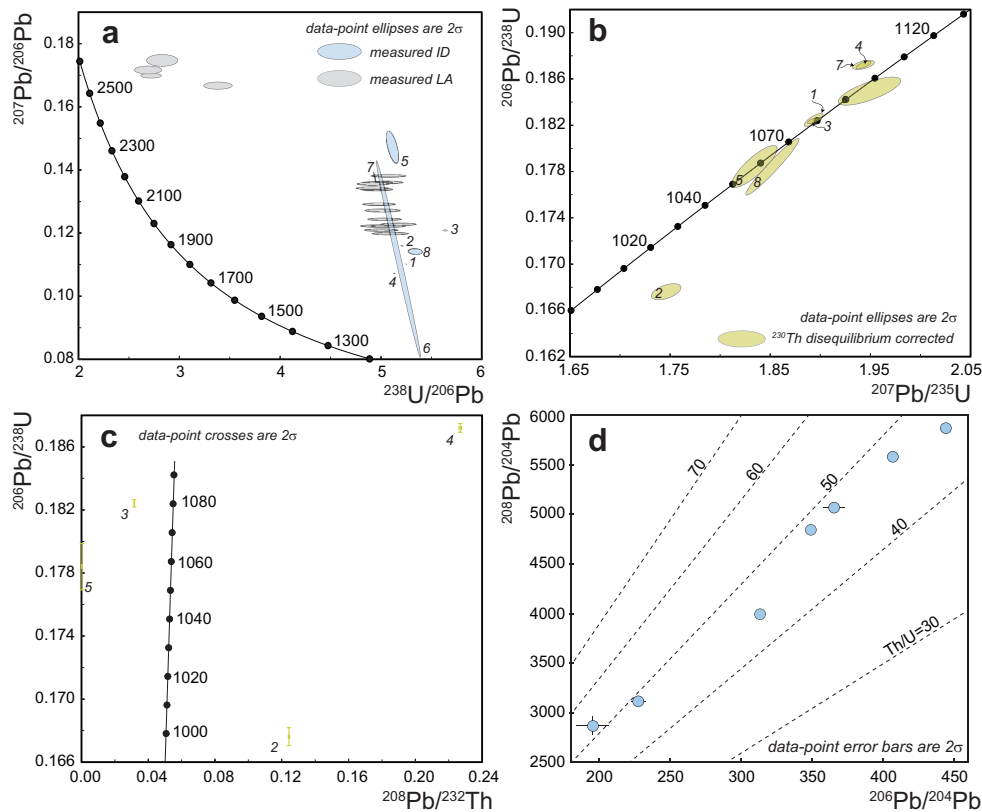


Fig. 5. U–Th–Pb ID and LA-ICPMS data for allanite LE2808. (a) Tera–Wasserburg Concordia diagram showing raw LA (grey ellipses) and ID analyses (blue ellipses). LA analyses are normalised to allanite LE40010. Concordia ages are in Ma and small italicised labels correspond to ID grain fraction notations. (b) Common-Pb-corrected U–Pb ID analyses plotted on a Wetherill concordia diagram. Analyses are corrected using a 1.075 Ga model-Pb composition (Stacey and Kramers, 1975) and $\text{Th}/\text{U}_{\text{whole-rock}} = 5$. The coordinates of grain 2 are consistent with post-crystallisation Pb-loss. (c) Common-Pb corrected U–Th–Pb ID data plotted on a $^{206}\text{Pb}/^{238}\text{U}$ – $^{208}\text{Pb}/^{232}\text{Th}$ concordia diagram. All analyses are discordant and suggest decoupling of ^{232}Th from daughter ^{208}Pb over length scales greater than the analysed grain diameter ($\sim 400 \mu\text{m}$). (d) Pb evolution diagram contoured for 1.075 Ga isochrons for allanite Th/U values between 30 and 70. Isochrons were calculated using initial $^{206}\text{Pb}/^{204}\text{Pb} = 16.93$ and initial $^{208}\text{Pb}/^{204}\text{Pb} = 36.62$ (Stacey and Kramers, 1975). (For interpretation of the references to colour in this figure legend, the reader is referred to the web version of this article.)

$^{208}\text{Pb}/^{232}\text{Th}$ ages (Fig. 5c), decoupling of Th from ^{208}Pb must have occurred relatively recently to account for the absence of a change in the Pb composition trajectory.

U–Pb LA data were normalised to allanite LE40010 and exhibit a bimodal distribution in Tera–Wasserburg space (Fig. 5a). The majority ($n = 13$) of analyses have values of $^{207}\text{Pb}/^{206}\text{Pb}$ between ~ 0.12 and ~ 0.14 and values of $^{238}\text{U}/^{206}\text{Pb}$ between ~ 4.9 and ~ 5.2 , similar to the dispersion exhibited by ID measurements. This group of LA analyses defines a trajectory that is consistent with 2-component mixing between a common-Pb end-member and radiogenic-Pb of ca. 1100 Ma; limited spread in $^{238}\text{U}/^{206}\text{Pb}$ space precludes calculation of statistically meaningful intercept values. Th–Pb isotopic data were not collected by LA-ICPMS.

4.3. Siss and Bona

U–Th–Pb isotopic analyses were performed on nine grains of Siss allanite selected from the same mineral separate used by von Blanckenburg (1992). Separated grains were dark brown, $<150\ \mu\text{m}$ diameter and screened for overgrowths of metamorphic epidote. Siss allanite exhibits a range in Th/U between 1 and 125, and contains ~ 30 – 50 mol.% non-radiogenic-Pb ($^{206}\text{Pb}/^{204}\text{Pb} = 20$ – 34 ; Table 1). Uncorrected U–Pb data are dispersed in a triangular-shaped topology when plotted in Tera–Wasserburg Concordia space (Fig. 6a), indicative of mixing between common-, radiogenic- and inherited-Pb components. The large spread of this data ($^{238}\text{U}/^{206}\text{Pb}$ values between 10 and 80) precludes calculation of a meaningful lower intercept age. Following correction for both common-Pb and excess- ^{206}Pb , six grains exhibit concordant $^{206}\text{Pb}/^{238}\text{U}$ and $^{207}\text{Pb}/^{235}\text{U}$ ages (Fig. 6b), between ~ 30 and 50 Ma. The remaining three discordant grains have $^{206}\text{Pb}/^{238}\text{U}$ ages between 40 and 264 Ma, and are characterised by markedly lower Th/U between 0.9 and 30.0. Plotted on a Wetherill Concordia diagram, the common-Pb-corrected data define a discordia (MSWD = 2.1) between an Alpine-age lower intercept and ~ 1 Ga (Fig. 6b). The antithetic relationship between discordance and Th/U shows that the U–Pb ID data comprise mixing between an inherited pre-Alpine, low Th/U component and an Alpine age, high Th/U component. When plotted on a $^{208}\text{Pb}/^{232}\text{Th}$ – $^{206}\text{Pb}/^{238}\text{U}$ Concordia diagram seven out of nine ID data points form a concordant to mildly discordant cluster between 28 and 32 Ma (Fig. 6c), whereas grains 8 and 6 contain significant amounts of inherited ^{206}Pb and ^{208}Pb . Using a value for Th/ U_{magma} of 5, correcting for excess- ^{206}Pb reduces $^{206}\text{Pb}/^{238}\text{U}$ ages by a maximum of 10% (grain 1). Relative to the amount of ^{208}Pb produced by radiogenic in-growth of the high Th/U Alpine component, the contribution of inherited ^{208}Pb is minor. This, together with the absence of intermediate daughter-product disequilibria, means that the Th–Pb system provides a more accurate and precise constraint on the age of Alpine magmatism: eight grains yield a mean corrected age of 30.18 ± 1.5 Ma (2σ), within uncertainty of the multi-grain fraction $^{208}\text{Pb}/^{232}\text{Th}$ age (30.10 ± 0.10 ; 2σ), measured by von Blanckenburg (1992), interpreted to represent the timing of allanite crystallisation. The remaining

grain contains a larger inherited component, yielding an age of 45.46 ± 1.6 Ma (2σ).

Single-spot LA-ICPMS U–Th–Pb analyses of Siss allanite were normalised to allanite LE40010. Plotted on a Tera–Wasserburg diagram, (Fig. 6a) data from three different grains of Siss allanite define a mixing chord (MSWD = 2.5; $n = 35$) between common-Pb that is significantly less radiogenic ($^{207}\text{Pb}/^{206}\text{Pb} = 0.8617 \pm 0.0088$, 95% conf.) than 30 Ma model-Pb predicted by Stacey and Kramers (1975), and a lower concordia intercept of 32.8 ± 1.20 Ma (2σ). The LA data show no sign of an inherited Pb component, suggesting that the pattern of inheritance present in ID data is caused by micro-inclusions of U-rich minerals such as zircon as opposed to inherited radiogenic-Pb distributed throughout the allanite lattice. On a linearised probability density plot, measured $^{208}\text{Pb}/^{232}\text{Th}$ ratios disperse along a line of slope 0.98 (± 0.16 , 95% conf.; Fig. 6f) corresponding to a mean value of 0.002470 ± 0.00095 (2σ). The data define an asymmetric distribution with a strong negative skew caused by common-Pb contamination.

Bona allanite yields Th/U values similar to Siss (36.5–156; Table 1) but has higher concentrations of common-Pb; only 7–17 mol.% ^{206}Pb is radiogenic ($^{206}\text{Pb}/^{204}\text{Pb} = 20$ – 23 ; Table 1). Uncorrected ID U–Pb analyses (Fig. 6d) disperse about a similar data topology to Siss allanite, indicating the presence of an inherited, pre-Alpine Pb component. The scatter in these data preclude determination of both an intercept age and initial common-Pb composition. Common-Pb corrected $^{206}\text{Pb}/^{238}\text{U}$ ages range between 22 and 55 Ma with propagated age uncertainties between 8% and 20% (2σ), reflecting the small U-load analysed. For this reason $^{207}\text{Pb}/^{235}\text{U}$ ages are not considered useful. Using the whole-rock Th/U value (1.587) measured by von Blanckenburg (1992), $^{206}\text{Pb}/^{238}\text{U}$ ages decrease by 5–12 Ma. Despite their low-precision, the data define a similar pattern of discordance to Siss allanite when plotted on a Wetherill concordia (Fig. 6e). In particular, grain 4 is discordant with a $^{206}\text{Pb}/^{238}\text{U}$ age of 55.19 ± 4.7 Ma (2σ) and has the lowest Th/U ratio (36.5). Grain 1 yields a $^{206}\text{Pb}/^{238}\text{U}$ age of 22.27 ± 3.1 Ma (2σ ; not corrected for excess- ^{206}Pb), significantly younger than the expected timing of crystallisation (von Blanckenburg, 1992). Such a young age can be explained by post-crystallisation Pb-loss.

Single-spot U–Pb LA-ICPMS analyses obtained from two Bona allanite grains were normalised to allanite LE40010 and define an isochron (MSWD = 14) between common-Pb with a $^{207}\text{Pb}/^{206}\text{Pb}$ value (0.8480 ± 0.021 95% conf.) within uncertainty of 30 Ma model-Pb composition (Stacey and Kramers, 1975) and a lower intercept age of 40.4 ± 4.8 Ma (2σ). Similar to Siss allanite, the absence of an inherited Pb signal in the LA U–Pb data shows that the included source of pre-Alpine Pb is unevenly distributed throughout the allanite grains. Uncorrected LA $^{208}\text{Pb}/^{232}\text{Th}$ ratios have a mean value of 0.0021 ± 0.00052 (2σ ; $n = 29$) and disperse along a slope of 0.96 ± 0.16 on a linearised probability density plot (Fig. 6f). The positive skew of the data distribution reflects heterogeneity in the relative concentrations of radiogenic- and common-Pb.

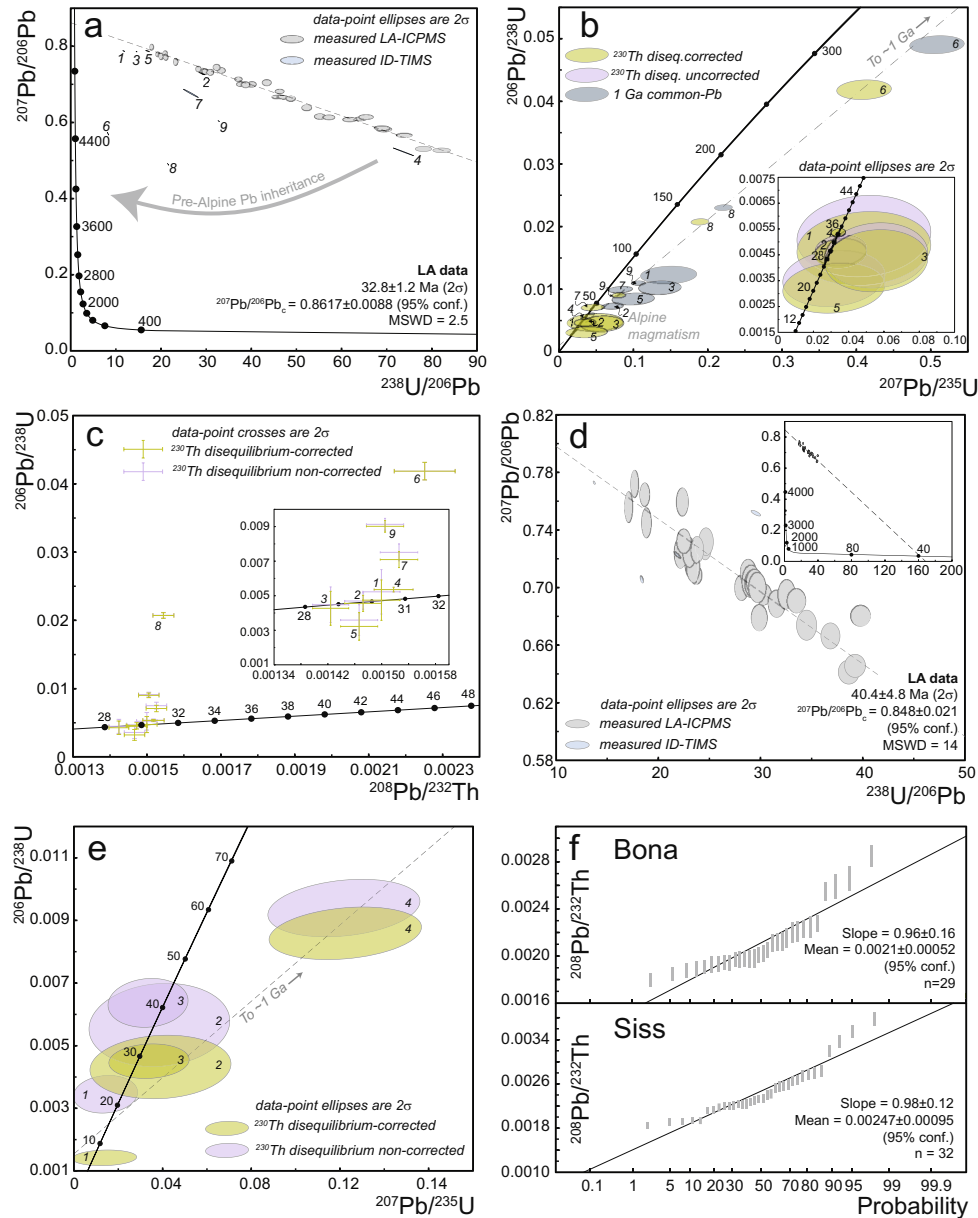


Fig. 6. U–Th–Pb ID and LA-ICPMS results for Siss and Bona allanite. (a) Tera–Wasserburg concordia showing raw LA (grey ellipses) and ID analyses (blue, numbered ellipses) of Siss allanite. LA data are normalised to allanite LE40010 and yield a coherent (MSWD = 2.5) isochron with a lower intercept of 32.8 ± 1.2 Ma (2σ). ID analyses show considerable dispersion, consistent with inheritance of a Pre-Alpine Pb component. (b) Common-Pb-corrected Siss allanite ID analyses plotted on a Wetherill concordia. Analyses are corrected using measured whole-rock Pb isotope compositions and Th/U of von Blanckenburg (1992); $^{208}\text{Pb}/^{204}\text{Pb} = 38.847$; $^{207}\text{Pb}/^{204}\text{Pb} = 15.679$; $^{206}\text{Pb}/^{204}\text{Pb} = 18.766$; $\text{Th}/\text{U}_{\text{whole-rock}} = 4.798$. Note that the signature of Pre-Alpine Pb inheritance is insensitive to incorporation of common-Pb of extreme composition, e.g. 1 Ga model Pb (Stacey and Kramers, 1975; blue ellipses). (c) Siss allanite ID analyses plotted on a $^{206}\text{Pb}/^{238}\text{U}$ – $^{208}\text{Pb}/^{232}\text{Th}$ concordia diagram. The pattern of discordance shows that the inherited component must be dominated by uranogenic Pb and low Th/U values. Insert displays close-up of concordant fractions and the magnitude of the excess- ^{206}Pb correction. (d) Tera–Wasserburg Concordia plot showing raw LA (grey ellipses) and ID analyses (light blue ellipses) of Bona allanite. LA data from multiple grains are normalised to allanite LE40010 and yield a lower intercept age of 40.4 ± 4.8 Ma (2σ); the data are not corrected for excess- ^{206}Pb . Inset shows the elevated concentrations of common-Pb typical of Bona allanite. Uncorrected ID analyses show considerable dispersion and do not form a statistically robust population. (e) Common-Pb-corrected Bona allanite ID analyses plotted on a Wetherill concordia. Analyses are corrected using measured whole-rock Pb isotope compositions and Th/U of von Blanckenburg (1992); $^{208}\text{Pb}/^{204}\text{Pb} = 38.862$; $^{207}\text{Pb}/^{204}\text{Pb} = 15.682$; $^{206}\text{Pb}/^{204}\text{Pb} = 18.805$; $\text{Th}/\text{U}_{\text{whole-rock}} = 1.587$. Note the similar signature of inheritance to Siss allanite. (f) Linearised probability plots of $^{208}\text{Pb}/^{232}\text{Th}$ LA data from multiple grains of Bona and Siss allanite. Analyses are normalised to allanite LE40010. (For interpretation of the references to colour in this figure legend, the reader is referred to the web version of this article.)

4.4. Tara

U–Pb ID analysis was performed on six grains of Tara allanite, five of which were used for Th–Pb ID. Analysed allanite grains show $^{206}\text{Pb}/^{204}\text{Pb}$ values between 41 and 194, and have a large range in Th/U, between 24 and 204 (Table 1). Uncorrected U–Pb ID analyses form a poorly-defined (MSWD = 83) array in Tera–Wasserburg coordinate space (Fig. 7a), intercepting concordia at 406.7 ± 8.2 Ma (2σ), within uncertainty of the accepted age of plutonism (412 ± 1.4 Ma, Williams et al., 1982). The data yield an initial $^{207}\text{Pb}/^{206}\text{Pb}$ common-Pb composition of 0.792 ± 0.039 (95% conf.)—more radiogenic than 420 Ma-old model Pb (0.864 ± 0.014 2σ ; Stacey and Kramers, 1975). Following correction for a 400 Ma common-Pb component (Stacey and Kramers, 1975), all grain fractions are concordant, or mildly reversely discordant on a Wetherill Concordia diagram between 400 and 440 Ma (Fig. 7b). The correction of excess- ^{206}Pb , using

$\text{Th}/\text{U}_{\text{magma}} = 5$, decreases $^{206}\text{Pb}/^{238}\text{U}$ ages by 0.7–7 Ma depending on both the age and Th/U of the allanite grain. Residual deviations from Concordia, such as grain 5, suggest inaccurate common-Pb or an underestimate of the initial magma Th/U value. Corrected $^{208}\text{Pb}/^{232}\text{Th}$ ages range between 329 and 414 Ma; grains 7, 6 and 9 are concordant in U–Th–Pb Concordia space (Fig. 7c). Despite being concordant in Wetherill coordinate space, grains 4 and 8 are reversely discordant ($^{208}\text{Pb}/^{232}\text{Th} < 0.0195$) in U–Th–Pb Concordia space, suggesting loss of thorogenic Pb, or heterogeneity in the initial common-Pb composition. The inset of Fig. 7c shows a Pb-evolution diagram on which all measured ID Pb data are plotted. With the exception of grain 8, which exhibits a low Th/U value of 24.48, all grain fractions disperse along a Pb-evolution array that is consistent with radiogenic in-growth of Pb from 420 Ma parent allanite with Th/U between 100 and 250. Notably, the data are consistent with closed-system Th/U behaviour in Tara allanite since the timing of formation.

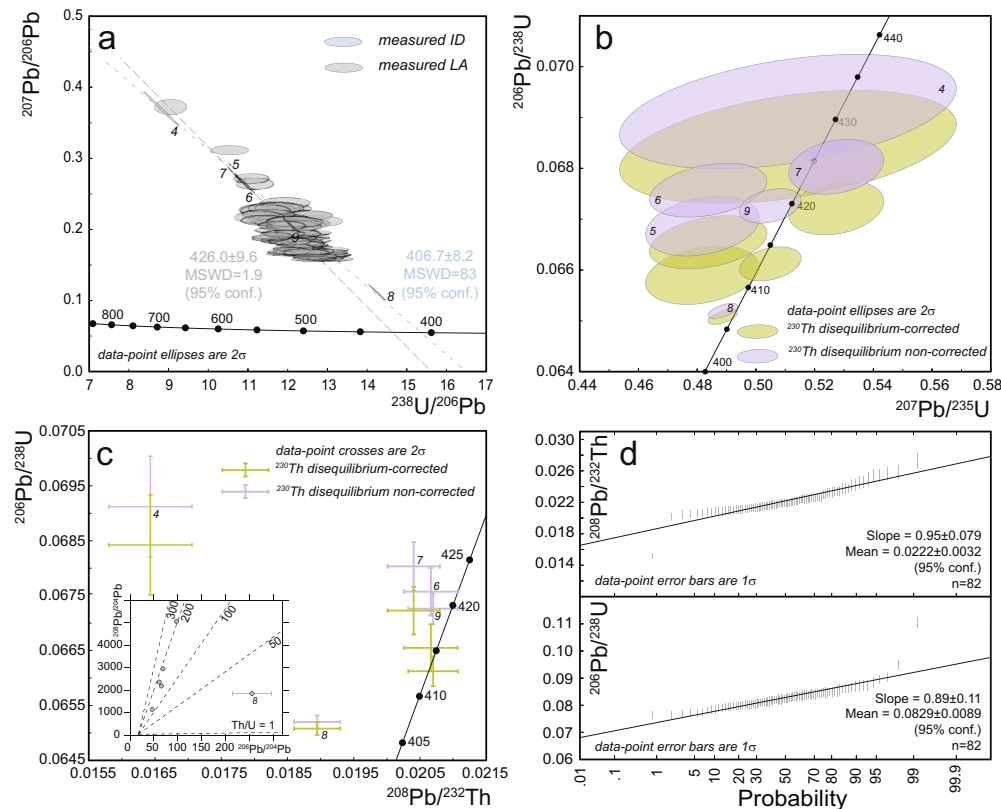


Fig. 7. U–Th–Pb ID and LA-ICPMS data for Tara allanite. (a) Measured LA (gray ellipses) and ID (blue ellipses) U–Pb data plotted on a Tera–Wasserburg concordia diagram. LA data are normalised to allanite LE40010 and were collected from two different grains; collectively, the data yield a lower intercept age of 426.0 ± 9.9 Ma (95% conf.; MSWD = 1.9). ID analyses show significant scatter (MSWD = 83) and yield a younger intercept age (406.7 ± 8.2 Ma, 95% conf.). The $^{207}\text{Pb}/^{206}\text{Pb}$ intercept of the LA data regression (0.879 ± 0.089 95% conf.) is consistent with 420 Ma model Pb (0.864 ± 0.014 2σ ; Stacey and Kramers, 1975), whereas the ID data define a more radiogenic $^{207}\text{Pb}/^{206}\text{Pb}$ intercept of 0.792 ± 0.039 (95% conf.). (b) Wetherill concordia diagram showing common-Pb-corrected U–Pb ID data (420 Ma common-Pb, Stacey and Kramers, 1975). All grain fractions plot concordant or sub-concordant between 400 and 440 Ma. The excess- ^{206}Pb correction uses $\text{Th}/\text{U}_{\text{whole-rock}} = 5$, and decreases $^{206}\text{Pb}/^{238}\text{U}$ ages by < 7 Ma. (c) $^{208}\text{Pb}/^{232}\text{Th}$ – $^{206}\text{Pb}/^{238}\text{U}$ concordia diagram showing common-Pb-corrected U–Pb ID data. Inset panel shows measured ID Pb analyses plotted on a Pb evolution diagram. Dashed-lines are isochrons calculated for 420 Ma Pb and values of Th/U between 1 and 400. (d) Measured LA $^{208}\text{Pb}/^{232}\text{Th}$ and $^{206}\text{Pb}/^{238}\text{U}$ ratios plotted on a linearised probability density diagram. Data points were collected from two grains of Tara allanite during three separate analytical sessions. (For interpretation of the references to colour in this figure legend, the reader is referred to the web version of this article.)

melting, pluton emplacement and magmatic differentiation. Inheritance in allanite has previously been observed (Romer and Siegesmund, 2003; Gregory et al., 2012), but is much less common than in zircon, presumably due to lower temperatures of allanite saturation and of Pb diffusion through the allanite lattice. The ability of allanite to resist complete loss of radiogenic Pb at upper amphibolite facies metamorphism has also been documented, suggesting that its closure temperature is in the ~ 650 °C range (Heaman and Parrish, 1991).

To date there are no experimentally-derived diffusion parameters available for allanite. Current understanding is based on the U–Th–Pb systematics of natural samples, relative to those observed in cogenetic zircon, monazite and titanite. Heaman and Parrish (1991) concluded that the retentivity of radiogenic-Pb in allanite exceeds titanite at upper amphibolite facies conditions. On the basis of differences in implied Pb-loss, the authors roughly estimated a closure temperature range of 650 ± 25 °C for allanite. This early estimate is at odds with the observation of Oberli et al. (2004), who calculated closure temperatures between 700 and 728 °C on the basis of a sequence of preserved excess- ^{206}Pb concentrations in allanite from the feeder zone of the Bergell pluton. Gregory et al. (2012) estimated closure temperatures between 620 and 700 °C based on the presence of Permian, xenocrystic cores to allanite grains that crystallised during Alpine migmatitisation, between 20 and 30 Ma, in the Central Alps. The presence of an inherited Pb component in Siss allanite is consistent with closure temperatures to Pb diffusion over lengthscales >150 μm that is similar to, or in excess of, the magmatic temperatures experienced, between 700 and 800 °C.

These allanite samples illustrate the potential difficulties involved when interpreting U–Pb data from young Th-rich phases. Similar to monazite (Copeland et al., 1988; Parrish, 1990), allanite grains may appear concordant due to a fortuitous combination of excess- ^{206}Pb forcing the data point above (Wetherill) concordia, whilst inherited Pb, or Pb loss, shifts the data point along a discordia towards an upper intercept with the concordia. Small signal intensities of ^{207}Pb , particularly apparent with single-crystal analysis, lead to imprecise $^{207}\text{Pb}/^{235}\text{U}$ measurements that will hinder the ability to deconvolve components of inheritance and ^{230}Th disequilibrium in such cases of young allanite.

5.2. Non-diffusive disturbance of the U–Th–Pb system in allanite

Empirically-derived constraints of Pb-diffusion in allanite shows that in all but the smallest grain sizes (<10 μm) and slowest cooling rates (<5 °C Ma^{-1}) from lower-crustal, or magmatic temperatures, solid-state volume diffusion cannot explain patterns of U–Th–Pb discordance in allanite (Heaman and Parrish, 1991). Rather, isotopic exchange between the mineral lattice and a grain-boundary fluid phase is energetically more favourable (e.g. Cole et al., 1983; Villa, 2006). Interface-coupled dissolution–precipitation is chiefly controlled by the degree of thermodynamic disequilibrium between fluid and reactant mineral. Following dissolution of the parent mineral surface,

super-saturation of the fluid phase results in epitaxial or polycrystalline precipitation, reflecting the degree of similarity between the crystallographic orientations of the parent and product phases. Surface energies and kinetics will act to limit the rate of solute exchange and the process will minimise the Gibbs free energy. Experimental data show that dissolution–precipitation of U and Th-bearing accessory minerals has the potential to effectively reset the U–Th–Pb chronometers even at temperatures <100 °C. Such data sets illuminate a critical dependence of the degree U, Th and Pb mobilisation on fluid composition; specifically, the alkali concentration of the fluid (Seydoux-Guil-laume et al., 2002; Budzyń et al., 2011; Williams et al., 2011; Krenn et al., 2012). Whereas phosphates appear to respond to hydrothermal alteration largely by preferential leaching of lattice-bound cations, including actinides and Pb, silicates show smaller degrees of chemical flexibility. Present understanding of the response of the U–Th–Pb allanite geochronometer to hydrothermal alteration is limited to a single study. Poitrasson (2002) showed that Carboniferous-age allanite from Corsican calc-alkaline and anorogenic granites responded to low-temperature (~ 100 °C) hydrothermal alteration by transformation to epidote and concomitant incorporation of Pb_c. Bulk-mineral REE and Sm–Nd isotopic signatures were not significantly affected.

Allanite LE40010 is a ca. 2.7 Ga pegmatite-hosted megacryst likely to have experienced multiple episodes of hydrothermal fluid interaction since the timing of crystallisation. Back scattered electron imaging reveals networks of fractures ranging from <1 μm to >500 μm in length adjacent to which the host allanite has been altered to clinozoisite–epidote with highly variable REE + Th contents (<0.3 –1 c.p.f.u.; Figs. 2a, 4 and 8). Fig. 4 shows that these altered domains exhibit disturbed U–Th–Pb isotopic compositions, characterised by a spread in $^{238}\text{U}/^{206}\text{Pb}$ values between 1.6 and 2.2 and $^{232}\text{Th}/^{208}\text{Pb}$ between 5.8 and 7.2. Altered domains are enriched in Ca and Al relative to pristine allanite. Further, the presence of uraninite (UO_2) as 1–5 μm -diameter patches within altered zones (Fig. 8) is strong evidence to suggest that U was mobilised during the hydrothermal alteration. Following dissolution of the host allanite grain, U released into the fluid will precipitate once saturation levels are attained. Loss of U plausibly explains the position of ID grain fractions a3 and j1 above Wetherill Concordia (Fig. 3b). However, given that Pb mobilisation likely occurred simultaneously, it is more accurate to interpret ID U–Pb data points as reflecting different proportions of Pb-loss/gain and U-loss/gain. Despite corrected ID analyses of LE40010 plotting along a discordia consistent with small fractions of radiogenic Pb-loss ($<10\%$; Fig. 3b), the absence of a correlation between grain size and degree of discordance further suggests that the U–Th–Pb discordance was caused by a non-diffusive process. These observations support the interpretation that fluid-induced dissolution–precipitation along fractures facilitated the transformation of allanite to epidote/clinozoisite, the incorporation of common-Pb and varying degrees of radiogenic-Pb loss.

However, the most striking feature of the U–Th–Pb ID data sets for allanites LE40010 and LE2808 is the apparent

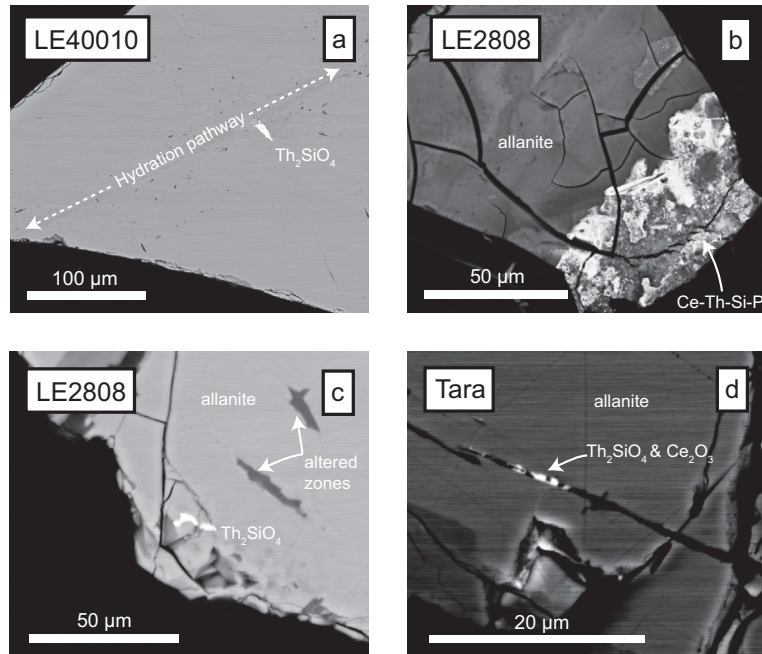


Fig. 8. High-contrast BSE SEM images of metasomatic Th-rich phases in hydrothermally-altered allanites. (a) LE40010. Note the presence of a hydration pathway discernable by lower BSE intensity, reflecting lower Th and higher Ca content. Dark flecks are SiO_2 inclusions. (b) LE2808. Grain fraction is heavily fractured, likely due to lattice swelling in response to self-irradiation. (c) LE2808. Thorite proximally associated with high-Ca patches and fractures. (d) Tara. Thorite and Ceria precipitates in-filling fractures.

decoupling of the U–Pb and Th–Pb systems. Allanite LE40010 exhibits ^{232}Th – ^{238}U age discordance ($[e^{(\lambda_{238}\text{Th})t} - 1]/[^{206}\text{Pb}/^{238}\text{U}] - 1$) between 7.1 (grain d3) and -0.91 (grain c2), whereas allanite LE2808 has values between 3.7 (grain 4) and -0.99 (grain 5). Tara allanite exhibits less extreme Th/U fractionation with ^{232}Th – ^{238}U age discordance between -0.24 (grain 4) and -0.02 (grain 6). In contrast to LE40010, allanite LE2808 displays concordant to subconcordant U–Pb systematics (Fig. 5b), indicating only minor uraniumic Pb-loss (grain fraction 2 LE2808) or disturbance of U. Such extreme discordance of the ^{232}Th – ^{208}Pb decay chain relative to the U–Pb system, characterised by the horizontal dispersal of data points in $^{208}\text{Pb}/^{232}\text{Th}$ – $^{206}\text{Pb}/^{238}\text{U}$ concordia space (Figs. 3c and 5c), reflects either preferential gain of ^{208}Pb , or loss of ^{232}Th . Given the larger atomic mass difference and markedly different chemical properties between Th and U and Pb, gain of ^{208}Pb is not considered a plausible explanation. This is supported by the Pb evolution plots shown in Figs. 3d and 5d which confirm that the Pb isotopic composition of allanites LE40010 and LE2808 has not been perturbed by significant in-growth of uraniumic or thorogenic Pb following fractionation of Th/U. The dispersion in $^{208}\text{Pb}/^{232}\text{Th}$ ages relative to corrected U–Pb ages must be caused by recent mobilisation of Th from the allanite lattice, in agreement with the fact that each of these allanites exhibit μm -scale inclusions of thorite (ThSiO_4), or ThO_2 , present as rounded to sub-angular patches and invariably associated with Ca-bearing fractures cutting pristine allanite (Fig. 8a–c). Thorite in allanite LE40010 is considerably more abundant than uraninite and occurs both as patches

<20 μm length adjacent to zones of high-Ca, and also as smaller (<5 μm diameter), rounded inclusions within the unaltered matrix. This correlation between size of the secondary Th-rich phase and the dimensions of the altered region is also observed in allanites LE2808 and, to a lesser extent, Tara. Such microtextures are consistent with coupled dissolution–reprecipitation of allanite behind an inwardly percolating hydrous fluid. Thorite precipitation in LE2808 and Tara is accompanied by crystallisation of Ce_2O_3 along fractures (Fig. 8c and d).

To account for the observed patterns of U–Th–Pb discordance, Th must have been mobilised over length-scales exceeding typical grain diameters (>300 μm). Individual grain fractions operated as open-systems to Th isotopic exchange between allanite and fluid. This is supported by Fig. 9, in which ^{232}Th concentrations measured by ID, LA and EPMA are plotted for each of the allanites considered. In general, concentrations measured by ID span a larger range and have average values than those measured by LA and EPMA. Given that ID analyses typically consume $10^{8-9} \mu\text{m}^3$ allanite, compared with $<10^5$ and $<5 \mu\text{m}^3$ for LA and EPMA, respectively, this confirms that selective removal of Th by hydrothermal fluids operated efficiently over single grain-fraction dimensions. The probability of producing mixed analyses of pristine and altered (Th-depleted) allanite is much greater in the case of ID.

Collectively, these observations show that allanite is susceptible to hydrothermal mobilisation of U, Th and LREE and accompanied enrichment in Ca and Al. Mobilisation of Th in response to partial chemical alteration driven by hydrothermal fluids has also been observed in monazite

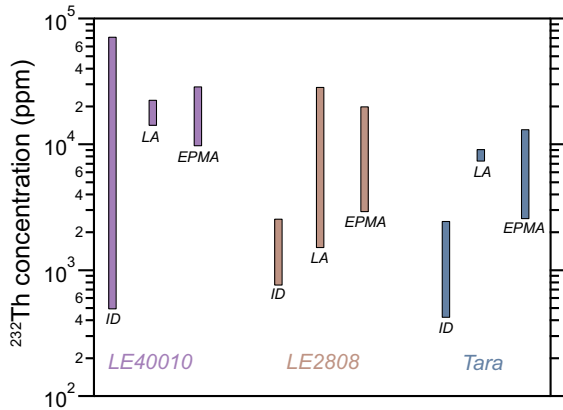


Fig. 9. ²³²Th concentrations of allanites LE40010, LE2808 and Tara measured by ID, LA-ICPMS and EPMA.

(Seydoux-Guillaume et al., 2002), xenotime (Hetherington and Harlov, 2008) and zircon (Geisler et al., 2002). In particular, Geisler et al. (2007) observe that hydrothermally-altered domains of zircon often exhibit elevated concentrations of non-formula elements such as Ca and Fe. Harlov and Hetherington (2010) exposed natural, unzoned, Th- and Pb-bearing monazite to Na-bearing aqueous fluid in piston cylinder apparatus at 1000 MPa and 900 °C. During the experiment Th was selectively removed from a subset of the monazite grains and subsequently incorporated in ThSiO₄-enriched monazite, devoid of Pb. This is in contrast to the allanite data presented here in that Pb appears to have been less mobile than Th during dissolution. Oelkers and Poitrasson (2002) showed that reprecipitation of Th as Th-rich secondary phases is strongly controlled by the pH of the fluid phase. Under high pH conditions, Th has demonstrably lower solubility than when exposed to acidic fluids. The presence of both ThO₂ and ThSiO₄ precipitates in allanites LE40010, LE2808 and Tara suggest differing degrees of SiO₂ saturation of the dissolving fluid phase.

5.3. Effects of self-irradiation damage

Pertinent to the interpretation of U–Th–Pb datasets is that the physical properties of mineral phases in the amorphous state will be drastically different to those in the crystalline state. Metamictization is accompanied by macroscopic swelling of the mineral lattice, reaching up to 16 volume% in Pu-doped zircon (Weber et al., 1994). Experimental studies show that mineral solubility and solid-state diffusivities of the host mineral grain are markedly higher when the lattice is disordered (Ewing et al., 1982, 2000; Ewing, 1999; Geisler et al., 2003), consistent with the strong correlation between degree of radiogenic Pb-loss and structural integrity based on a wealth of U–Th–Pb isotopic data from natural samples (Silver and Deutsch, 1963; Wasserburg, 1963; Pidgeon et al., 1966; Goldich and Mudrey, 1972; Mezger and Krogstad, 1997; Geisler et al., 2002). However, in contrast to monazite and zircon, little is known concerning the response of U–Th–Pb isotope systematics to metamictization in allanite.

Fig. 10a shows the estimated self-irradiation doses for ID grain fragments from allanites LE40010, LE2808 and Tara, plotted against ²³²Th–²³⁸U age discordance (Fig. 10 caption for definition). Siss and Bona are excluded from consideration due to the effects of chemical inheritance discussed above. Calculated self-irradiation doses are based on the mean, common-Pb corrected ²⁰⁶Pb/²³⁸U age and the actinide concentrations derived by ID analysis. Grain fractions of allanite LE40010 received doses between $\sim 2 \times 10^{16}$ and $\sim 3 \times 10^{18}$ α -decay g⁻¹. Importantly, the degree of discordance increases above cumulative dose values of $\sim 3 \times 10^{17}$ α -decay g⁻¹ from values close to unity to between 0 and 5. Beneath this value, discordance varies unsystematically and is ± 0.1 . With the exception of one outlier, grain fractions of allanite LE2808 all received cumulative doses in excess of 3×10^{17} α -decay g⁻¹ and plot between 0 and 4.2 discordant, reflecting the high concentrations of Th present in the sample and its ca.1.075 Ga age. Grain fractions of Tara allanite cluster around Th–Pb Concordia

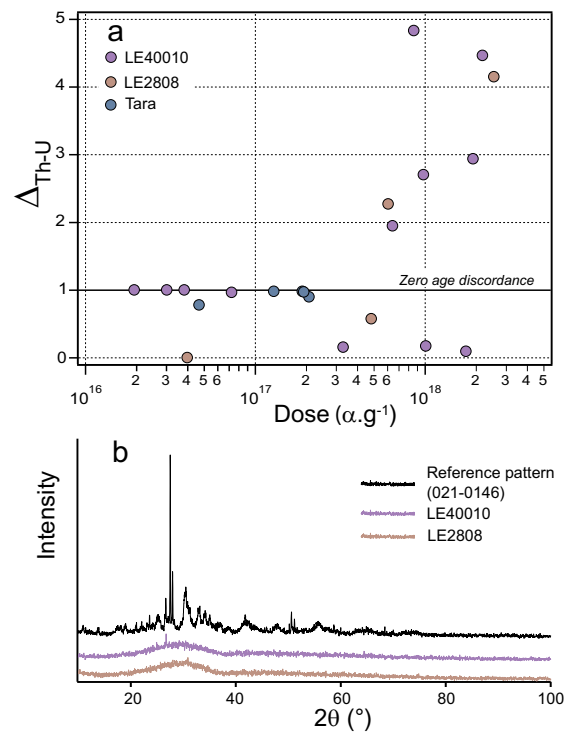


Fig. 10. Effects of self-irradiation damage on U–Th–Pb systematics of allanite. (a) Plot of cumulative dose versus discordance ($\Delta_{\text{Th-U}} = [e^{t_m/\lambda_{232}} - 1] / [e^{t_r/\lambda_{238}} - 1]$), where t_m is the measured ²⁰⁸Pb/²³²Th age and t_r is the mean ²⁰⁶Pb/²³⁸U age, calculated for each ID grain fraction. Cumulative dose (α -decays g⁻¹) is calculated using: $D = 8N_{238}[e^{t_r/\lambda_{238}} - 1] + 7N_{235}[e^{t_r/\lambda_{235}} - 1] + 6N_{232}[e^{t_r/\lambda_{232}} - 1]$, where N corresponds to the number of parent atoms present. Solid horizontal line represents ²⁰⁸Pb/²³²Th–²⁰⁶Pb/²³⁸U age concordance. Grain fractions with values of $\Delta_{\text{Th-U}} > 1$, have lost Th, whereas grains with $\Delta_{\text{Th-U}} < 1$ reflect Pb-loss or Th-gain; 2σ uncertainties are less than the marker dimensions. (b) Powder XRD patterns for allanites LE40010 and LE2808 plotted against allanite reference pattern 021-0146. Minor peak at 26° in LE40010 spectrum reflects the presence of quartz inclusions.

at dosage values between 4×10^{16} and 2×10^{17} α -decay g^{-1} . The dose–discordance relationships exhibited by allanites LE40010 and Tara are consistent with the explanation that increasing structural disorder in the allanite lattice elevates the susceptibility of the grain to dissolution-driven Th/U fractionation and facilitates faster rates of diffusive Pb-loss. More specifically, the topology of the LE40010 data points suggest that a percolation threshold is passed at cumulative dose values close to 3×10^{17} α -decay g^{-1} , an order of magnitude smaller than the dose required for the first percolation point in zircon (Salje et al., 1999) and current estimates for the dose required to induce amorphization of the allanite lattice ($3.2\text{--}10 \times 10^{18}$ α -decay g^{-1} ; Janeczek and Eby, 1993). Powder XRD experiments show that allanites LE40010 and LE2808 are both pervasively metamict (Fig. 10b). XRD spectra are characterised by broad bulges between 20 and 40° 2θ , caused by incoherent scattering of X-rays by amorphous material; the small amounts of Tara allanite available precluded XRD analyses.

Despite the strong correlation between accumulated radiation dose and U–Th age discordance, it is important to note that this relationship is also a function of the geological history experienced by each allanite grain. Specifically, the dose calculations for allanites LE2808, LE40010 and Tara yield estimates of the total dose received since crystallization. In the case where hydrothermal alteration occurred recently, such as is the case for allanites LE40010 (Fig. 3d) and LE2808 (Fig. 5d), this assumption is valid; however, should an alteration event have occurred at an intermediate stage during the history of the sample, the actual dose received would be smaller. Also, given their Precambrian formation ages, it is likely that allanites LE40010 and LE2808 experienced temperatures in excess of 380 °C for durations greater than 1 Ma at some point during their histories, facilitating the onset of self-annealing of accumulated radiation damage (Saini et al., 1975; Janeczek and Eby, 1993).

Petrographical imaging reveals that altered regions of allanites LE40010, LE2808 and Tara contain zones of enrichment in both Th and U relative to unaltered allanite (Fig. 8). As documented previously by Gindy (1961) and Poitrasson (2002), the elevated actinide concentrations in these domains will increase the self-irradiation doses received by regions of adjacent allanite. In turn, these regions will become more susceptible to further alteration and Pb-loss leading to a positive feedback between radiation damage accumulation and alteration.

6. IMPLICATIONS FOR ALLANITE GEOCHRONOLOGY

The susceptibility of allanite to common-Pb contamination and extreme Th/U fractionation has immediate implications for the methodology employed to extract meaningful chronometric information. Because allanite commonly preserves micrometer-scale gradients in U, Th and Pb, *in situ* isotopic analysis by either SIMS or LA-ICPMS is preferred over ID analysis for the extraction of intragrain ages (Gregory et al., 2007; Gabudianu Radulescu et al., 2009; Janots et al., 2009; Rubatto et al., 2011) which

will yield a grain-volume integrated age. Accurate U–Th–Pb geochronology by LA-ICPMS and SIMS techniques critically relies on correcting measured isotopic ratios for elemental and isotopic mass fractionation incurred predominantly at the site of analysis, and also during mass and energy separation during mass spectrometry (Hirata and Nesbitt, 1995; Horstwood et al., 2003; Jackson et al., 2004). This correction is typically performed by application of a matrix normalisation factor, $R_{\text{known}}/R_{\text{measured}}$ (where R is the ratio of interest), calculated from repeated measurement of a reference material of known U–Th–Pb isotopic composition. Accordingly, the total uncertainty of *in situ* allanite geochronology is limited by the precision and accuracy to which the isotopic composition of the allanite reference material is known and its extent of homogeneity; after propagation of systematic uncertainties, any sample allanite cannot have an uncertainty less than the reference material to which it is corrected.

6.1. Matrix normalisation factors

Laser-induced elemental fractionation is caused by processes occurring at the ablation site and its magnitude changes throughout an ablation. The causes of elemental fractionation include differing atomic bond strengths, fluid-dynamic effects of gas flow within the ablation pit and the relative transport behaviour of analysed elements. In general, the more refractory element is preferentially retained within the ablation pit (Horn et al., 2000). Traditionally, it has been argued that laser induced elemental fractionation is minimised by matching the matrix composition and structure of both the reference and sample materials (e.g. Morrison et al., 1995; Catlos et al., 2000; Gregory et al., 2007; Chew et al., 2011). Recently, however, the importance of matrix structure in reducing elemental fractionation has been called into question with several studies suggesting that a dynamic ablation protocol eliminates the need to correct for depth-dependent fractionation (Storey et al., 2006; Darling et al., 2012b). However, despite reducing ablation depth, a final correction must still be applied to match the expected isotopic composition and given that the final age uncertainty is dominated by internal reproducibility, the use of rasters seems to only offer an advantage when analysing the most homogenous standards. Accordingly, we only consider matrix effects incurred using single spot analyses.

The ubiquitous presence of common-Pb in allanite complicates its use as a primary reference material. Variable concentrations of non-radiogenic Pb cause variations in both the $^{207}\text{Pb}/^{206}\text{Pb}$ and $^{206}\text{Pb}/^{238}\text{U}$ ratios that must be corrected prior to normalisation against the reference value, leading to additional uncertainty which must be propagated through the age calculation. To date, a satisfactory method of deriving primary normalisation factors from materials containing common-Pb has not been developed. This makes assessing the effects of matrix structure and composition on Pb/Pb and U/Pb fractionation a challenging task. In order to isolate the magnitude of such effects, we calculate the relative differences in Pb/U fractionation factors between those derived from LA-ICPMS U–Pb analyses of the

Siss allanite normalised to allanite LE40010, Stern monazite (Palin et al., 2013) and the 91500 zircon standard (Wiedenbeck et al., 1995). The fractionation factors for each of the different reference matrices are then assessed relative to those derived from the same Siss U–Pb dataset that correspond to a Tera–Wasserburg lower-intercept $^{206}\text{Pb}/^{238}\text{U}$ age in agreement with the ID data (32.7 Ma, average of grains without inheritance, uncorrected for excess- ^{206}Pb). For the reference case, Pb/Pb fractionation factors derived from analyses of either NIST612 glass (<1% deviation from expected value), or zircon 91500 (<1.1%) were used because of the fact that any matrix effects are insignificant relative to the instrumental mass bias ($\sim 1\%$ a.m.u. $^{-1}$). The Siss allanite data were collected during two analytical sessions.

The results for each analytical session are plotted in Fig. 11 as Tera–Wasserburg Concordia diagrams. With the exception of the case where Stern monazite is used as a primary standard, the session $^{207}\text{Pb}/^{206}\text{Pb}$ intercept value is identical to within uncertainty (95% conf.), irrespective of the mineral matrix employed as a primary standard. In Fig. 11a, the correct lower-intercept U–Pb age for Siss allanite

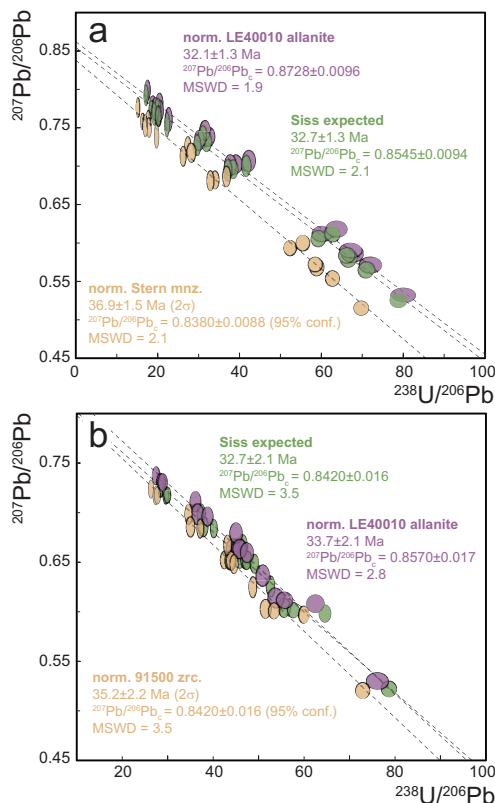


Fig. 11. Dependency of U–Pb fractionation correction on mineral matrix. (a) Siss allanite ($n = 17$) normalised to Stern monazite and allanite LE40010 all analysed in the same analytical session. Green analyses (Siss expected) represent the case where fractionation factors were derived to yield an age identical to the average ID age (32.7 Ma); (b) Siss allanite ($n = 16$) normalised to zircon 91500 and LE40010, compared to the reference case (green ellipses). Error ellipses are 2σ . (For interpretation of the references to colour in this figure legend, the reader is referred to the web version of this article.)

is reproduced using a Pb/U fractionation factor of -7.5% . Using allanite LE40010, Pb/Pb and Pb/U fractionation factors are -2% and -6% , respectively, whereas Stern monazite yields factors of -2% and -18% . In Fig. 11b, the reference age for Siss allanite corresponds to a Pb/U fractionation factor of $+2.5\%$. Using allanite LE40010, Pb/Pb and Pb/U factors are -0.16% and -0.17% , respectively; zircon 91500 yields factors of $+1.2\%$ and -4.9% . These calculations highlight two important points. Firstly, Pb/U fractionation factors calculated using allanite LE40010 provide the most accurate normalisation. Relative to allanite, the monazite matrix leads to Pb/U fractionation that is an order of magnitude larger (10.5% relative to 1.5%). However, given that the internal reproducibility of $^{207}\text{Pb}/^{206}\text{Pb}$ and $^{206}\text{Pb}/^{238}\text{U}$ for Stern monazite was 0.92% and 1.26%, respectively, a small component of the difference in Pb/U fractionation is attributable to common-Pb and sample heterogeneity. The relative difference in Pb/U is less extreme between zircon 91500 and allanite LE40010—approximately a factor of three. Collectively, this suggests that matrix effects are a significant source of Pb/U fractionation during LA analysis, in support of previous investigations (Gregory et al., 2007). Secondly, the internal reproducibilities of $^{207}\text{Pb}/^{206}\text{Pb}$ and $^{206}\text{Pb}/^{238}\text{U}$ for allanite LE40010 during the two runs are between 2.29–2.75% and 1.11–1.40% respectively, considerably larger than 0.4% and 0.53% for zircon 91500 and also Stern monazite. The greater degree of dispersion reflects the presence of heterogeneous quantities of common-Pb in allanite LE40010. This dispersion is propagated onto individual data point uncertainties, reducing the degree of scatter (MSWD) of the Tera–Wasserburg regression and the uncertainty of the final lower-intercept age estimate. Therefore, despite accurate fractionation correction, the elevated internal reproducibility of allanite LE40010 could lead to decreased levels of final age precision.

The high Th/U ratios common to allanite means that ages derived from the ^{232}Th – ^{208}Pb system are less sensitive to common-Pb correction than those derived from the U–Pb decay chains; further, unlike $^{206}\text{Pb}/^{238}\text{U}$ ages, the ^{232}Th – ^{208}Pb decay chain is not affected by initial disequilibrium. The calculated Pb/Th fractionation factor for Stern monazite is $+2.9\%$, considerably lower than the values calculated from Tara ($+58$ – 129%), Siss ($+25.9$ – 73%) and LE40010 ($+51.2$ – 90.4%). Internal reproducibilities of measured $^{208}\text{Pb}/^{232}\text{Th}$ ratios are 8.7–9% for NIST612 glass, 1.03% for Stern monazite, 1.5–5.2% for Tara allanite, 14.4–21.0% for Siss allanite and 2–3.95% for allanite LE40010. Clearly, the allanite Pb/Th ratios are more strongly fractionated than the Pb/U ratios, which cannot be explained by instrumental mass fractionation alone ($\sim 1\%$ a.m.u. $^{-1}$). Kohn and Vervoort (2008) suggest that elevated Pb/Th fractionation factors calculated from monazite standard materials could be caused by differences in vaporization temperatures, ($\text{Pb} < \text{U} < \text{Th}$, Guillon and Günther, 2002), either at the site of ablation or within the plasma. Although mass-dependent processes occurring at the ablation site will contribute to the magnitude of the fractionation factor, sample heterogeneity, chiefly governed by the distribution of common-Pb and the accuracy

of the reference ID-TIMS data, will dominate the accuracy of the correction. The elevated internal reproducibilities for allanite $^{208}\text{Pb}/^{232}\text{Th}$ ratios attest to the presence of variable amounts of common-Pb, further evidenced by uncorrected ID data for Siss (25.87% RSE $^{208}\text{Pb}/^{232}\text{Th}$, 1 outlier) and Tara (8.55% RSE $^{208}\text{Pb}/^{232}\text{Th}$). Allanite LE40010 displays a more coherent distribution of common-Pb (1.46% RSE $^{208}\text{Pb}/^{232}\text{Th}$, grain A), but its use as a primary standard for $^{208}\text{Pb}/^{232}\text{Th}$ normalisation would require isotopic characterisation of individual grains.

6.2. Uncertainty propagation

Traditionally, three sources of error are considered in the uncertainty evaluation of *in situ* U–Th–Pb data: the internal measurement uncertainty, limited by counting statistics for measurements on linear detection systems; the internal reproducibility of a population of isotopic measurements, usually expressed as the RSE; the accuracy of the fractionation correction, determined by the isotopic and elemental homogeneity of the reference material. Typically, single-point measurement uncertainties for the $^{207}\text{Pb}/^{206}\text{Pb}$ ratio are limited to $\sim 0.2\text{--}0.3\%$ (2σ) using ion counters, whereas elemental $^{206}\text{Pb}/^{238}\text{U}$ and $^{208}\text{Pb}/^{232}\text{Th}$ ratios are reproduced at the percent level ($\sim 2\text{--}3\%$ 2σ). Accordingly, the largest component of uncertainty pertains to the calibration of the inter-element ratio which relies on the assumption that all analyses of the reference material have the same isotopic composition and do not exhibit variations due to factors such as common-Pb, Pb-loss or Th/U disequilibrium. Whilst zircon reference materials justify this assumption, exhibiting $< 0.1\%$ (2σ), and $< 0.4\%$ (2σ) variation in Pb/Pb and Pb/U ratios, respectively (Wiedenbeck et al., 1995), the U–Th–Pb ID data presented here show that variance in allanite Pb/Pb and U/Pb ratios is significant, typically an order of magnitude larger than zircon. This reflects the cumulative effects of high and variable common-Pb content, inheritance, excess- ^{206}Pb and Th/U fractionation. Dispersal in the U–Th–Pb isotopic composition directly affects the accuracy of the fractionation correction and therefore must be propagated into the final uncertainty estimate. We consider this a source of systematic uncertainty which must be added in quadrature to any individual age estimate such that no age can have an uncertainty less than the ability to reproduce the reference allanite Pb/Pb, Pb/Th or Pb/U ratio. This is preferred over propagating the uncertainty onto individual data points so as not to obscure real scatter in the data population. Accordingly, the ID data show that U–Pb ages for allanites LE40010, LE2808, Siss and Tara cannot be known to better than 5% (1 RSE, $n = 5$), 3.8% (1 RSE, $n = 8$), 37% (1RSE, $n = 5$) and 16% (1RSE, $n = 6$); whereas, Th–Pb ages are limited to 1.4% (1 RSE, $n = 4$, grain A), 104% (1 RSE, $n = 4$), 18% (1 RSE, $n = 6$, grains devoid of inheritance) and 3.7% (1 RSE, $n = 4$), respectively. Clearly, the large degree of scatter precludes the use of many of these allanites as primary standards for U–Pb and Th–Pb geochronology.

6.3. Common-Pb correction

Due to the similar ionic radii of Ca^{2+} and Pb^{4+} , allanite has a propensity to incorporate large amounts of non-radiogenic Pb on crystallisation or equilibration. In turn, the final age uncertainty is sensitive to errors in estimates of the initial concentration of common-Pb present. Using ID-TIMS analysis, it is possible to accurately measure ^{204}Pb and subsequently correct sample ratios by assigning an initial common-Pb composition and projecting towards concordia an amount proportional to the magnitude of measured $^{207}\text{Pb}/^{204}\text{Pb}$, $^{206}\text{Pb}/^{204}\text{Pb}$ and $^{208}\text{Pb}/^{204}\text{Pb}$. Using this method, the allanites investigated vary in common-Pb proportions from Siss ($\text{Pb}^*/\text{Pb}_c = 0.36\text{--}2.17$) and Bona ($\text{Pb}^*/\text{Pb}_c = 0.68\text{--}1.66$), which have the highest proportions of non-radiogenic Pb, to LE40010 ($\text{Pb}^*/\text{Pb}_c = 72\text{--}349$) which, due to its old age, hosts minute proportions of common-Pb. However, measurement of ^{204}Pb is hampered in plasma-ionisation source mass spectrometry due to isobaric interferences pertaining to the presence of ^{204}Hg in the carrier gas and the fact that ^{204}Pb is the least abundant Pb isotope. In the case that ^{204}Pb cannot be measured, common-Pb correction can be accomplished by assuming U–Pb concordancy, nominating a common-Pb composition and calculating the amount of common-Pb from the measured ^{207}Pb . This method requires an estimate of the sample age and is most accurate for Phanerozoic samples where the range in radiogenic $^{207}\text{Pb}/^{206}\text{Pb}$ is large compared to the range in $^{206}\text{Pb}/^{238}\text{U}$ (Williams, 1998). Alternatively, the radiogenic $^{208}\text{Pb}/^{206}\text{Pb}$ ratio can be estimated from the sample $^{232}\text{Th}/^{238}\text{U}$ ratio by assuming both that Th/U in the sample has remained undisturbed and an estimate for the sample age (Compston et al., 1984). This correction is most applicable to low Th/U samples (Williams, 1998). However, given that allanite is rarely concordant in U–Pb concordia coordinate space and commonly exhibits extreme fractionation of Th/U, these assumptions likely incur considerable inaccuracy.

For the U–Pb system, the Tera–Wasserburg Concordia diagram offers the most suitable method to assess the U–Pb systematics of common-Pb-bearing allanite. A data point array that yields an MSWD close to unity confirms that the Pb isotopic composition results from two-component mixing between radiogenic and common end-members, both of which can be extracted from the lower concordia intercept and the intercept with the $^{207}\text{Pb}/^{206}\text{Pb}$ axis, respectively. Importantly, an MSWD of unity does not mean that there is no geological scatter in the data set; rather, it means that the dataset is consistent with two-component mixing at the level of analytical precision. If accurate ^{204}Pb measurements are available (e.g. ID-TIMS) the $^{204}\text{Pb}/^{206}\text{Pb}$ ratio can be incorporated into a 3-D, or Total Pb–U isochron, which allows full propagation of the covariance of U–Pb uncertainties and more precise age and common-Pb estimates (Levchenkov and Shukolyukov, 1970; Wendt, 1984; Ludwig, 1998, 2003a; Storey et al., 2006).

Laser ablation analyses of the Siss and Tara allanites (Figs. 6a and 7a) disperse along linear regressions in Tera–Wasserburg Concordia space with MSWDs of 2.5

and 1.9, respectively. Such low levels of U–Pb scatter along with the correspondence between extrapolated $^{207}\text{Pb}/^{206}\text{Pb}$ and model or measured Pb compositions, support the application of a ^{207}Pb -based common-Pb correction. Fig. 12a and b shows the results of this correction applied to 36 spot analyses of Tara allanite and 35 spot analyses of Siss allanite each collected over two analytical sessions. Using allanite LE40010 as a primary standard, Tara yields a weighted mean $^{206}\text{Pb}/^{238}\text{U}$ age of 415.9 ± 2.9 Ma from a population of corrected analyses with $\text{MSWD} = 1.4$ (Fig. 12a). This age is within 2σ uncertainty of both the SHRIMP zircon U–Pb (Ickert and Williams, 2011) and Rb–Sr reference ages (Williams et al., 1982), confirming the suitability of the ^{207}Pb -based correction scheme. The results from Siss are less convincing, however, with corrected spots yielding a weighted mean age of 27.6 ± 1.5 Ma (2σ), considerably younger than the ID $^{208}\text{Pb}/^{232}\text{Th}$ and $^{206}\text{Pb}/^{238}\text{U}$ ages presented here and those obtained from previous studies (von Blanckenburg, 1992). The elevated MSWD (70) shows that the common-Pb composition is heterogeneous over intra-grain lengthscales, leading to overcorrection and artificially young ages; furthermore, the ages displayed in Fig. 12b are not yet corrected for the effects of excess- ^{206}Pb . Given that Siss allanite has greater than 80% common- ^{206}Pb , small variations in the common-Pb composition will propagate into large inaccuracies in the final corrected age. Accordingly, free regression of uncorrected $^{207}\text{Pb}/^{206}\text{Pb}$ and

$^{238}\text{U}/^{206}\text{Pb}$ ratios is critical to justify application of the ^{207}Pb -based correction.

The absence of a second decay chain to assess concordancy makes graphical analysis of uncorrected Th–Pb data problematic. Previous studies employ the ^{207}Pb -based correction scheme to estimate the fraction of non-radiogenic ^{208}Pb from the measured $^{208}\text{Pb}/^{206}\text{Pb}$ ratio (Gregory et al., 2007, 2012; Janots et al., 2009; Rubatto et al., 2011). However, such an approach assumes that Th/U of the analyte has remained undisturbed, which is often not the case for allanite (e.g. Figs. 3c, 5c and 7c). Therefore, it is important to assess the degree of Th/U fractionation before employing such a correction. Fig. 12c and d shows LA Th–Pb data from Tara and Siss allanites plotted on a ^{232}Th – ^{208}Pb isochron using measured ^{206}Pb as the reference isotope. The low degree of scatter ($\text{MSWD} = 1.4$) exhibited by Tara analyses indicates that Th/U fractionation is small at the level of analytical precision, whereas the data from Siss allanite exhibit considerable scatter, consistent with variable Th/U. In this case, the low MSWD values from Tara would justify application of the ^{207}Pb -based correction, whereas by doing so with the Siss data would incur considerable inaccuracy. Similar assessment of the Th/U fractionation can also be performed using a Pb-evolution plot ($^{208}\text{Pb}/^{206}\text{Pb}$ versus $^{207}\text{Pb}/^{206}\text{Pb}$). Further work is required to refine a three-dimensional numerical correction procedure (Anderson, 2002) using measured $^{232}\text{Th}/^{208}\text{Pb}$, $^{208}\text{Pb}/^{206}\text{Pb}$ and Th/U ratios.

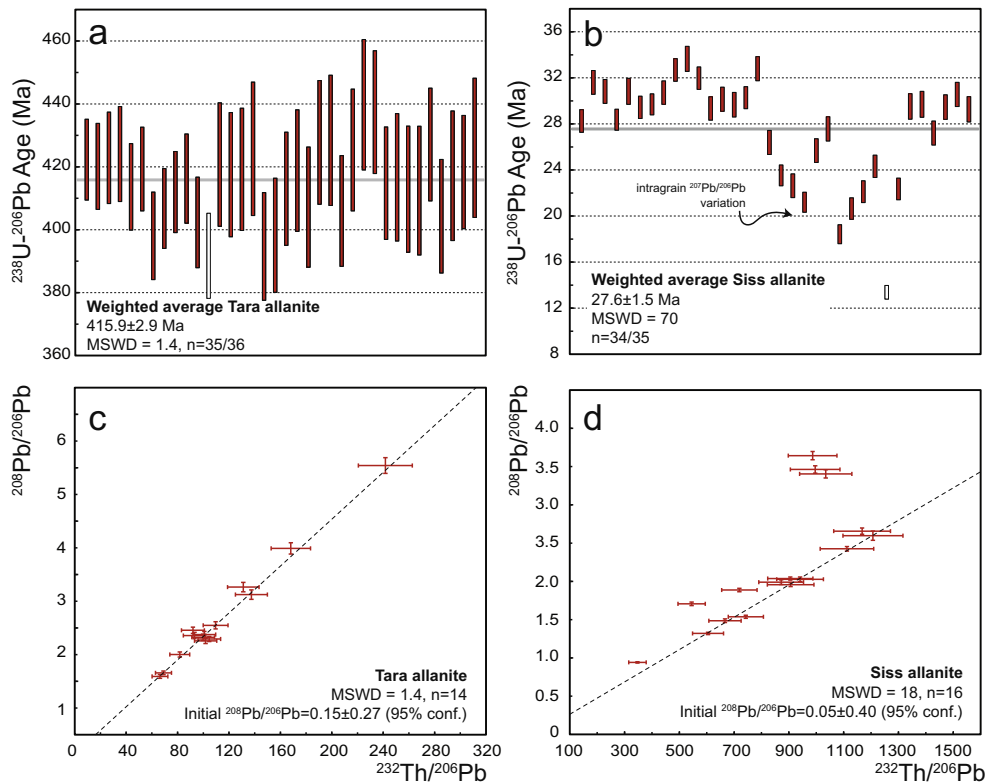


Fig. 12. Common-Pb correction. LA-ICPMS single-spot corrected $^{206}\text{Pb}/^{238}\text{U}$ ages for (a) Tara, and (b) Siss allanites, using allanite LE40010 as a primary standard. Error box heights correspond to 2σ . Clear boxes are excluded from the age calculation. The lower panels show uncorrected Th–Pb isochrons for (c) Tara and (d) Siss allanites. Error crosses are 2σ .

6.4. The effect of initial ^{230}Th disequilibrium

The propensity of allanite to sequester Th over U means that samples crystallizing from a reservoir with a low Th/U ratio may be affected by the production of unsupported ^{206}Pb from ^{230}Th , an intermediate daughter nuclide of the ^{238}U decay series ($t_{1/2} \approx 76$ ka). This results in artificially old $^{206}\text{Pb}/^{238}\text{U}$ ages, relative to $^{207}\text{Pb}/^{235}\text{U}$ and $^{208}\text{Pb}/^{232}\text{Th}$ ages (Schärer, 1984), which will be greatest in young (<30 Ma) samples where there is insufficient radiogenic ^{206}Pb to dilute excess- ^{206}Pb . The age excess can be corrected by either assuming prior knowledge of the reservoir Th/U ratio, often taken to be the same as the whole-rock Th/U, or, if better constrained, values for the U and Th partition coefficients. However, the Th/U ratio of a crystallising magma evolves over time, predominantly controlled by the mass fraction of Th and U removed from the melt by accessory phases, which means that measured whole-rock values do not necessarily correspond to the Th/U ratio in the magma at the time of allanite formation. Petrographic relations show that allanite saturation and subsequent crystallisation occur early within melt differentiation, explaining the characteristic LREE depletion of felsic magmas (Miller and Mittlefehldt, 1982; Gromet and Silver, 1983; Bea, 1996). In the case where melt differentiation occurred by fractional crystallisation, the whole-rock Th/U ratio provides a minimum estimate of the Th/U ratio of the magma at the time of allanite formation. Oberli et al. (2004) quantified $^{230}\text{Th}/^{238}\text{U}$ disequilibrium relationships in zoned allanite from the Bergell pluton to reveal a smooth, initially steep, decrease of Th/U in the host magma from values of 2.9 at 32 Ma to < 0.1 at 28 Ma. Because the Th/U of the melt in equilibrium with early allanite is > 3 times higher than the measured whole-rock value (0.79), allanite must have undergone fractional crystallisation early within the evolution of the melt, verified by accompanying whole-rock Sm-Nd isotopic data. The high temperatures required for allanite melt saturation is supported by the experimental data of Hermann (2002) who shows that allanite is a residual phase up to temperatures between 900 and 1000 °C for metabasalts and metasediments, respectively, at <10% partial melting. The same study estimates partition coefficients ($D_{\text{all-melt}}$) for Th and U between allanite and a hydrous granitic melt at 900 °C and 2.0 GPa as 60 and 20, respectively ($D_{\text{Th}}/D_{\text{U}} = 3$).

The Siss, Bona and Tara allanites all require correction for excess- ^{206}Pb , whereas the old ages (>1 Ga) of LE40010 and LE2808 allanites preclude the need for a correction. Details of the ^{230}Th disequilibrium-corrected $^{206}\text{Pb}/^{238}\text{U}$ ages for each ID analysis of Tara, Siss and Bona allanites are listed in Table 2. Fig. 13a and b shows the sensitivity of the corrected $^{206}\text{Pb}/^{238}\text{U}$ age to a range of likely Th/ U_{magma} from which Siss and Tara allanites crystallised, respectively. Each curve corresponds to a selected ID analysis (Table 1). Assuming that the Th/ $U_{\text{whole-rock}}$ accurately represents a minimum estimate of the Th/U ratio from which the allanite crystallised, analyses of Siss allanite are insensitive to the chosen value of Th/ U_{magma} above 4.79 (von Blanckenburg, 1992). This is supported by agreement between the average $^{208}\text{Pb}/^{232}\text{Th}$ age and analyses 1–3 for

values of $\text{Th}/U_{\text{magma}} > \text{Th}/U_{\text{whole-rock}}$. Given the young age of the Siss allanite, the magnitude of the correction is controlled by the high Th/ $U_{\text{whole-rock}}$ value reported by von Blanckenburg (1992); were the effective Th/ U_{magma} ratio to be similar to the range reported by Oberli et al. (2004), age corrections > 1 Ma would be expected. Given that Th/U in selected Siss allanite grains varies between 6 and 89, effective Th/ $U_{\text{magma}} > 4.79$ correspond to values of $D_{\text{Th}}/D_{\text{U}} < 18.5$.

Elevated Th/U values for Tara allanite, typically between 128 and 204, mean that the magnitude of the age correction is strongly dependent on Th/ U_{magma} (Fig. 13b). Unfortunately there are no published Th/ $U_{\text{whole-rock}}$ values available for the Tara granodiorite. Typical Th/ $U_{\text{whole-rock}}$ values for granodiorites are between 1 and 2 (e.g. von Blanckenburg, 1992), leading to $^{206}\text{Pb}/^{238}\text{U}$ age corrections > 5 Ma. Further, the ‘true’ $^{208}\text{Pb}/^{232}\text{Th}$ age spans ~13 Ma at 2σ uncertainty, providing only a loose constraint on the plausible range of effective Th/ U_{magma} . In such an underdetermined system, accurate propagation of uncertainties through the excess- ^{206}Pb correction is best performed using a Monte Carlo simulation. Values of Th/ U_{magma} are drawn from a pyramidal distribution spanning 1–10 with a mean value of 5.5, selected to represent the typical range in observed Th/ U_{magma} . Fig. 13c illustrates the results of such a calculation in which Tara allanite grain 6 is subjected to 10^6 correction calculations, generating the spread in corrected $^{206}\text{Pb}/^{238}\text{U}$ ages displayed in the inset panel. The minor difference between mean (417.36 Ma) and median (417.72 Ma) age values highlights negative skew in the age distribution. Results of Monte Carlo simulations are displayed in Table 2. Importantly, this approach accounts for likely variation in Th/ U_{magma} for which accurate values are difficult to constrain.

In the case where ^{204}Pb cannot be measured accurately, the excess- ^{206}Pb correction is hampered by interdependence of the $^{207}\text{Pb}/^{206}\text{Pb}$ ratio used in the common-Pb correction and the $^{206}\text{Pb}/^{238}\text{U}$ ratio used in the ^{230}Th disequilibrium calculation. In the presence of excess- ^{206}Pb , the commonly adopted ^{207}Pb -based common-Pb correction (Williams, 1998) will lead to an overestimate of the common ^{206}Pb fraction, the size of which will decrease with increasing common-Pb concentrations. The presence of excess- ^{206}Pb can be elucidated from the topology of U–Pb data in Tera–Wasserburg Concordia coordinate space. Whereas incorporation of a common-Pb component displaces analyses towards the $^{207}\text{Pb}/^{206}\text{Pb}$ axis, excess- ^{206}Pb displaces analyses towards the origin, reflecting the fact that excess- ^{206}Pb is thorogenic. Accordingly, the Pb composition of any analysis reflects three-component mixing between radiogenic, common and excess end-members. Fig. 13d shows the effect of different proportions of excess- ^{206}Pb on the topology of U–Pb LA data collected from Siss allanite (Fig. 6a). Contours were calculated assuming that the free regression line (MSWD = 2.5; common $^{207}\text{Pb}/^{206}\text{Pb} = 0.8617$; $^{206}\text{Pb}/^{238}\text{U}$ age = 32.8 Ma) represents mixing between radiogenic and common-Pb only (i.e. 0% excess- ^{206}Pb). Importantly, this plot highlights the fact that misfits between individual analyses and the 0% excess- ^{206}Pb contour do not correlate with Th/U ratio,

Table 2
Initial ^{230}Th disequilibrium correction.

Fractions ^a	$^{206}\text{Pb}/^{238}\text{U}$ age ^b (Ma)	$2\sigma^c$ (Ma)	$^{208}\text{Pb}/^{232}\text{Th}$ age ^d (Ma)	$2\sigma^c$ (Ma)	Corrected for excess ^{206}Pb				
					t mean ^e (Ma)	t median ^e (Ma)	$2\sigma^c$ (Ma)	$\Delta_{\text{Th-U}}^f$ (Ma)	$2\sigma^c$ (Ma)
<i>SISS</i>									
Allanite 1	33.60	8.29	30.29	0.56	30.44	30.50	8.83	0.15	9.39
Allanite 2	30.19	3.09	29.74	0.55	29.32	29.33	3.22	−0.42	3.77
Allanite 3	28.81	6.64	28.76	0.54	27.52	27.53	6.75	−1.24	7.30
Allanite 4	34.46	0.86	30.65	0.58	34.40	34.40	0.87	3.75	1.45
Allanite 5	23.10	5.74	29.62	0.56	21.67	21.69	5.91	−7.95	6.47
Allanite 6	264.29	8.24	45.46	1.67	264.23	264.23	7.92	218.78	9.59
Allanite 7	48.23	3.16	30.81	0.56	44.16	44.47	5.08	13.34	5.64
Allanite 8	132.43	2.67	31.20	0.57	130.98	131.04	3.01	99.79	3.58
Allanite 9	58.60	2.22	30.40	0.56	57.06	57.14	2.70	26.67	3.26
<i>Bona</i>									
Allanite 1	36.44	7.00	–	–	34.45	34.48	7.24	–	–
Allanite 2	40.97	4.11	–	–	37.55	37.73	5.30	–	–
Allanite 3	22.23	3.17	–	–	18.76	19.00	4.65	–	–
Allanite 4	60.35	4.83	–	–	59.62	59.63	4.86	–	–
<i>Tara</i>									
Allanite 4	430.85	5.93	329.38	6.35	428.01	428.09	6.22	98.63	12.57
Allanite 5	417.23	3.08	–	–	413.24	413.56	4.87	–	–
Allanite 6	421.52	2.80	413.42	4.10	417.36	417.72	4.83	3.94	8.93
Allanite 7	424.30	2.84	408.26	3.99	420.96	421.21	4.22	12.70	8.21
Allanite 8	407.17	0.77	379.38	3.53	406.70	406.73	0.92	27.32	4.45
Allanite 9	419.65	1.79	414.07	3.80	415.05	415.57	4.79	0.97	8.60

^a Single grain fractions, labelled for sample and allanite grain number.

^b Corrected for fractionation, spike and common Pb; not corrected for initial radioactive disequilibrium in $^{230}\text{Th}/^{238}\text{U}$.

^c Errors are 2σ , propagated using the algorithms of Schmitz and Schoene (2007).

^d Corrected for fractionation, spike, and common Pb (see beneath).

^e Calculated from Monte Carlo experiment using 10^6 data points, normally-distributed uncertainties assigned to isotopic measurements and a pyramid distribution between 1 and 10 (mean = 5.5) assigned to the $\text{Th}/\text{U}_{\text{magma}}$ ratio; fractionation factor, $f = (\text{Th}/\text{U})_{\text{allanite}}/(\text{Th}/\text{U})_{\text{magma}}$ (Schärer, 1984).

^f Difference between corrected $^{206}\text{Pb}/^{238}\text{U}$ and $^{208}\text{Pb}/^{232}\text{Th}$ ages, calculated using $(^{206}\text{Pb}/^{238}\text{U})_{\text{age}} - (^{208}\text{Pb}/^{232}\text{Th})_{\text{age}}$.

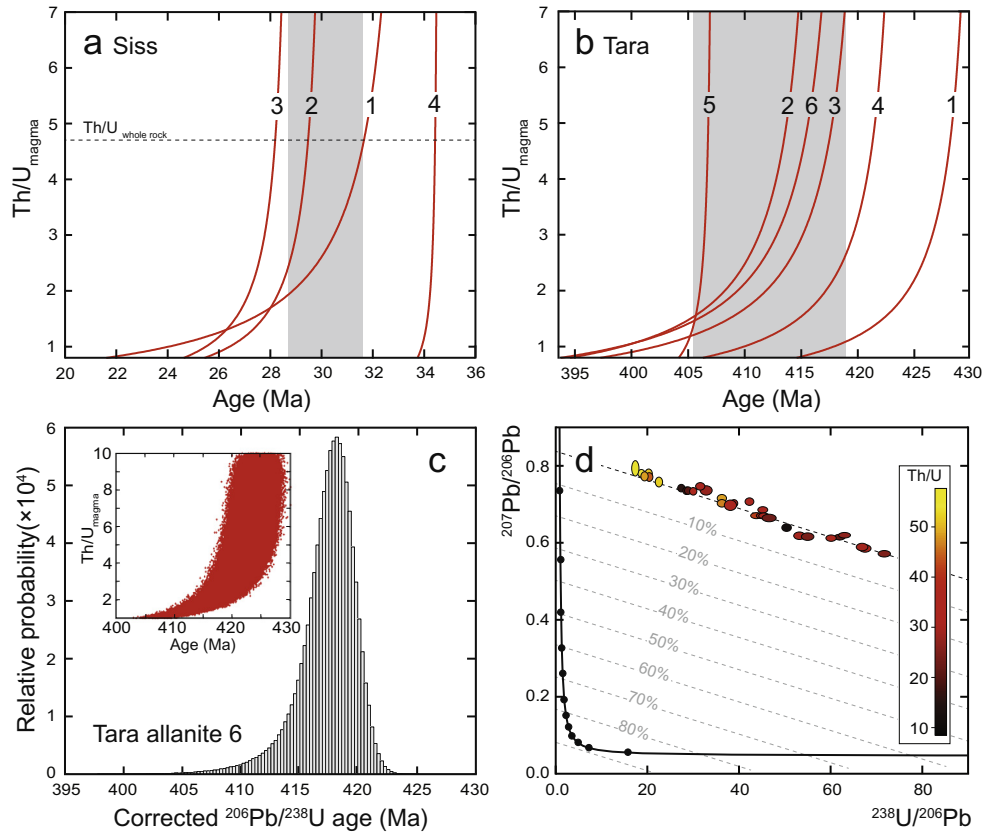


Fig. 13. The effect of ^{230}Th disequilibrium on corrected $^{206}\text{Pb}/^{238}\text{U}$ age. Panels (a) and (b) show the effect of varying $\text{Th}/\text{U}_{\text{magma}}$ ratio on $^{206}\text{Pb}/^{238}\text{U}$ age for selected ID-TIMS analyses from Siss and Tara allanites, respectively. Shaded rectangles represent average ID $^{208}\text{Pb}/^{232}\text{Th}$ ages and respective 2σ uncertainty intervals (Siss: 30.18 ± 1.56 Ma, $n = 8$; Tara: 411.92 ± 6.36 Ma, $n = 3$). Curves are labelled for grain numbers. Note the negligible sensitivity of Siss allanite grains to $\text{Th}/\text{U}_{\text{magma}}$ values in excess of the measured $\text{Th}/\text{U}_{\text{whole-rock}}$ value (4.79; von Blanckenburg, 1992). Panel (c) shows a histogram (100 bins) of corrected $^{206}\text{Pb}/^{238}\text{U}$ ages calculated for Tara grain 6 using a Monte Carlo approach ($n = 10^6$) in which $\text{Th}/\text{U}_{\text{magma}}$ is permitted to vary between 1 and 10 within a pyramid distribution (mean = 5.5). Normal distributions are adopted for the allanite isotopic composition. Inset shows the relationship between $\text{Th}/\text{U}_{\text{magma}}$ and corrected age for individual Monte Carlo data points. Panel (d) shows uncorrected LA data for Siss allanite plotted on a Tera–Wasserburg diagram, contoured for different amounts of excess- ^{206}Pb between 0% and 90% of total ^{206}Pb . Contours calculated using values of common and radiogenic $^{207}\text{Pb}/^{206}\text{Pb}$ determined by free regression of the data (Fig. 6a). Note that the magnitude of misfit between individual data points and the 0% line does not correlate with Th/U .

confirming the minor contribution of excess- ^{206}Pb to total- ^{206}Pb . U–Pb data collected from Alpine monazite exhibit topologies indicative of three-component mixing (Janots et al., 2012). Accurate correction of such data for both excess- ^{206}Pb and common-Pb components is best implemented using a Monte Carlo simulation in which the dependence of both the radiogenic and common-Pb end-member compositions on excess- ^{206}Pb is expressed as a probability distribution.

6.5. Pb/U versus $^{208}\text{Pb}/^{232}\text{Th}$ ages

The strong tendency for allanite to partition Th over U means that the uncertainty component related to counting statistics is smaller for $^{208}\text{Pb}/^{232}\text{Th}$ ages relative to $^{206}\text{Pb}/^{238}\text{U}$ ages and that the contribution of common ^{208}Pb relative to radiogenic ^{208}Pb is smaller compared to uraniumic Pb. Furthermore, the longest-lived intermediate

daughter nuclide in the ^{232}Th decay chain is ^{228}Ra ($t_{1/2} = 5.75$ a), meaning that $^{208}\text{Pb}/^{232}\text{Th}$ ages are not affected by intermediate isotopic disequilibrium. For these reasons the Th–Pb system has been preferentially targeted in previous allanite dating studies (von Blanckenburg, 1992; Barth et al., 1994; Oberli et al., 2004; Villa, 2006; Gregory et al., 2007; Rubatto et al., 2011).

However, the rarity of allanite Th–Pb ID data has led to the tendency to assume U–Th–Pb concordancy, not only in matrix-matched standard normalisation, but also through application of the ^{207}Pb -based common-Pb correction. The ID data presented here for allanites LE40010, LE2808 and, to a lesser extent, Tara, show that ^{232}Th can be strongly fractionated from U as well as from ^{208}Pb (Figs. 3c, 5c and 7c), implying that U–Th–Pb concordancy is the exception and not the rule, using the materials characterised in this study as representative samples of real allanites. Given the lack of a second decay chain, accurate age

Table 3
Target U–Th–Pb isotopic ratio values.

	$^{207}\text{Pb}/^{206}\text{U}$	2σ	$^{206}\text{Pb}/^{238}\text{U}$	2σ	$^{208}\text{Pb}/^{232}\text{Th}$	2σ
LE40010	0.2199 ^a	0.0127	0.5340 ^a	0.0155	0.1439 ^a	0.0041
Siss	0.8617 ^b	0.0088	0.005101 ^c	0.0002	0.002812 ^a	0.0007
Bona	0.8480 ^b	0.0210	0.006287 ^c	0.0002	–	–
Tara	0.7920 ^b	0.0390	0.06512 ^c	0.0013	0.02100 ^a	0.0002

^a Average value of uncorrected ID data, excluding outliers ($n = 10$ for LE40010 U–Pb composition; $n = 4$ for LE40010 $^{208}\text{Pb}/^{232}\text{Th}$; $n = 8$ for Siss $^{208}\text{Pb}/^{232}\text{Th}$; $n = 4$ for Tara $^{208}\text{Pb}/^{232}\text{Th}$).

^b Upper-intercept value of Tera–Wasserburg plot. Siss and Bona ratios calculated from LA data; Tara ratio calculated from ID data.

^c Lower-intercept value of Tera–Wasserburg plot. Siss and Bona ratios calculated from LA data; Tara ratio calculated from ID data.

data cannot be extracted from singular measurement of the Th–Pb system. Rather, paired U–Pb isotopic measurements provide an important means by which to assess Th/U fractionation. Further, allanite Pb/Th fractionation factors derived here are considerably larger and more variable than Pb/U fractionation factors reflecting both variability in the Pb/Th composition of the standard allanites and potential mass-independent factors such as matrix chemistry (Gregory et al., 2012) and vaporization temperatures (Kohn and Vervoort, 2008).

7. ARE ANY OF THESE ALLANITES SUITABLE AS REFERENCE MATERIALS FOR *IN SITU* ALLANITE GEOCHRONOLOGY?

The characteristics required from an ideal reference material for both SIMS and LA-ICPMS U–Th–Pb dating are low variance in the dispersion of measured U–Th–Pb isotopic compositions. This is the case for closed-system zircons and monazites that are concordant (Wiedenbeck et al., 1995; Sláma et al., 2008). However, for allanite and other common-Pb-bearing minerals such as titanite and apatite, where common-Pb is significant, the necessary characteristics are extended to include an array of U–Th–Pb data between a closed-system allanite and a common-Pb reservoir with a standard deviation, not standard error or weighted mean, of the projected age on such an array having less than $\sim 4\%$ uncertainty, and with the ID-TIMS U–Th–Pb composition known to better than 2–4%. Despite variable concentrations of common-Pb and the effects of Th/Pb fractionation, several of the allanites we have characterised here are suitable as reference materials for either U–Pb or Th–Pb geochronology. For future use, target U–Th–Pb isotopic ratio values for each allanite are presented in Table 3. In the following paragraphs, we make recommendations, presented in order of suitability, for the use of each allanite as reference materials for microbeam U–Th–Pb geochronology. Inherent to the future use of these standards in microbeam allanite U–Th–Pb geochronology is the optic to neglect outlier, or suspect, analyses caused by alteration and inclusions.

Allanite LE40010 exhibits $<2\%$ (1σ) dispersion in U–Pb isotopic composition attributable to the presence of common-Pb (Fig. 3a). Despite the fact that hydrothermally-altered regions display increased levels of dispersion in U–Pb, and particularly Th–Pb isotopic composition, with adequate prior characterisation of individual shards, LE40010 has the potential

to be used as both a U–Pb and Th–Pb reference material for allanite geochronology. Excluding outliers (Table 3), allanite LE40010 exhibits the smallest degree of common-Pb variability and affords the benefit of being able to derive primary Pb/U and Pb/Pb fractionation factors from single ratios, neglecting the requirement to coanalyse zircon or NIST glass. Evidence for extreme Th/Pb fractionation in allanite LE40010 is limited to micro-meter scale domains of hydration alteration and inclusions of thorite. Unaltered shards, such as grain A, exhibit $\sim 3\%$ dispersion in Th/Pb isotopic composition, suitable for primary normalisation of Th/Pb ratios.

Tara allanite has limited dispersion in measured U–Pb composition by LA and yields an uncorrected $^{206}\text{Pb}/^{238}\text{U}$ age consistent with the known crystallisation age, whereas the Th–Pb system exhibits considerable scatter caused by heterogeneous common-Pb compositions and open-system behaviour (Fig. 7a and c). Accordingly, we recommend that Tara allanite is used as either a primary U–Pb allanite standard, provided that Pb/Pb fractionation factors are derived from coanalysed zircons, as in Section 6.1, or as a secondary U–Pb reference material.

The suitability of Siss allanite as a primary U–Pb standard is compromised by an inherited Pb component. Whilst LA analyses normalised to LE40010 yield an uncorrected $^{206}\text{Pb}/^{238}\text{U}$ age within uncertainty of the accepted $^{208}\text{Pb}/^{232}\text{Th}$ age of the allanite (von Blanckenburg, 1992; Gregory et al., 2007), ID data are highly scattered (Fig. 6a). However, given the limited dispersion of the LA U–Pb data and spatially-restricted nature of the inherited Pb component, well characterised grains of Siss allanite are suitable for use as a secondary U–Pb reference material. Higher concentrations of radiogenic Pb mean that the Th–Pb system shows smaller degrees of scatter and is more suitable as a reference value following correction for common-Pb. Similar to Siss, the limited dispersion of Bona LA U–Pb data means that it is a suitable secondary reference material. Further work is required to resolve the nature of the inherited, pre-Alpine Pb signature. Allanite LE2808 exhibits dispersion in excess of 10% (1σ) for both U–Pb and Th–Pb isotopic compositions measured by both ID and LA-ICPMS making it unsuitable as a reference material.

8. CONCLUSIONS

Using both ID-TIMS and LA-ICPMS techniques, we have characterised the U–Th–Pb systematics of five allanite

samples, including the Siss, Bona and Tara allanites, currently in use as standards for microbeam allanite U–Th–Pb geochronology. Both Siss and Bona allanites are found to include an inherited Pb component attributable to either the presence of xenocrystic core domains, or the presence of zircon microinclusions. The presence of old allanite cores in allanite from the Bergell intrusion is consistent with previous observations that solid-state Pb diffusion through the allanite lattice must operate over lengthscales shorter than $\sim 300\ \mu\text{m}$ at temperatures and timescales less than 700–800 °C and ≤ 5 Myr, respectively. Despite being strongly retentive of Pb against volume diffusion, two pegmatite hosted allanite megacrysts, LE40010 and LE2808, exhibit disturbed U–Th–Pb isotope systematics, reflecting interaction with crustal fluids. Allanite megacryst LE40010 experienced extreme Th/U fractionation to yield apparent $^{208}\text{Pb}/^{232}\text{Th}$ ages >9 Ga. Allanites Tara and LE2808 also exhibit evidence for mobilisation of Th over length scales comparable to grain diameters (300–500 μm). Micrometer-scale precipitates of thorite, and rare uraninite provide physical evidence for dissolution–precipitation reactions during fluid-driven alteration. Dose–discordance relationships exhibited by allanites LE40010, LE2808 and Tara are consistent with the explanation that increasing structural disorder in the allanite lattice elevates the susceptibility of the grain to dissolution-driven Th/U fractionation and facilitates faster rates of diffusive Pb-loss. These calculations also suggest that allanite is affected by a percolation point at $\sim 3 \times 10^{17}$ α -decay g^{-1} , an order of magnitude smaller than determined for zircon.

We show that Pb/Pb, U/Pb or Th/Pb ratios obtained from single grains vary by $>4\%$ (2σ) for each of the allanites considered. This provides a limiting uncertainty in the use of these materials as allanite standards for *in situ* geochronology. Furthermore, the U–Th–Pb isotopic data presented suggest that allanite rarely fulfils the commonly-assumed condition of U–Th–Pb concordancy, meaning that it is important to evaluate both U–Pb and Th–Pb ages before correcting for common-Pb. We confirm the importance of matrix composition on the magnitude of laser induced elemental fractionation for allanite and show that Pb/U fractionation factors are consistently smaller than those derived for Pb/Th fractionation. We propose that allanite LE40010 is a suitable primary reference material for allanite U–Th–Pb geochronology. However, its effective use is critically dependent on screening individual shards for chemical alteration. Tara allanite is favoured over Siss and Bona allanites as a secondary U–Pb reference material or a primary reference material provided that Pb/Pb fractionation factors can be derived from zircon. Siss allanite is best suited for use as a Th–Pb reference material.

ACKNOWLEDGEMENTS

A.J.S. is in receipt of a Jackson Postdoctoral Fellowship and was supported by the NIGL during the analytical phase of this project. Constructive reviews from Martin Engi and two anonymous reviewers served to greatly improve the quality of the manuscript. Trevor Ireland is thanked for his efficient editorial handling. Daniela Rubatto and John Cottle are thanked for their help in acquiring

and supplying allanite reference materials Siss, Bona and Tara. Katie Gunderson performed XRD measurements and Antoni Milodowski supervised SEM analysis. This work has benefited from discussions and correspondence with Steve Noble, Noah Mclean, Katie Gunderson, Rod Ewing and Joe Hiess.

APPENDIX A. SUPPLEMENTARY DATA

Supplementary data associated with this article can be found, in the online version, at <http://dx.doi.org/10.1016/j.gca.2014.03.021>.

REFERENCES

- Anderson T. (2002) Correction of common lead in U–Pb analyses that do not report ^{204}Pb . *Chem. Geol.* **192**(1–2), 59–79.
- Barth S., Oberli F. and Meier M. (1994) Th–Pb versus U–Pb isotope systematics in allanite from co-genetic rhyolite and granodiorite: implications for geochronology. *Earth Planet. Sci. Lett.* **124**(1), 149–159.
- Bea F. (1996) Residence of REE, Y, Th and U in granites and crustal protoliths; implications for the chemistry of crustal melts. *J. Petrol.* **37**(3), 521–552.
- Beard J., Sorensen S. and Gieré R. (2006) REE zoning in allanite related to changing partition coefficients during crystallization: implications for REE behaviour in an epidote-bearing tonalite. *Mineral. Mag.* **70**(4), 419–435.
- Boundy T., Donohue C., Essene E., Mezger K. and Austrheim H. (2002) Discovery of eclogite facies carbonate rocks from the Lindås Nappe, Caledonides, Western Norway. *J. Metamorph. Geol.* **20**, 649–667.
- Broska I., Petrik I. and Williams C. T. (2000) Coexisting monazite and allanite in peraluminous granitoids of the Tribec Mountains, Western Carpathians. *Am. Mineral.* **85**(1), 22–32.
- Budzyń B., Harlov D. E., Williams M. L. and Jercinovic M. J. (2011) Experimental determination of stability relations between monazite, fluorapatite, allanite, and REE-epidote as a function of pressure, temperature, and fluid composition. *Am. Mineral.* **96**(10), 1547–1567.
- Catlos E., Sorensen S. S. and Harrison T. M. (2000) Th–Pb ion-microprobe dating of allanite. *Am. Mineral.* **85**(5–6), 633–648.
- Senki-Tok B., Oliot E., Rubatto D., Berger A., Engi M., Janots E., Thomsen T., Manzotti P., Regis D. and Spandler C. (2011) Preservation of Permian allanite within an Alpine eclogite facies shear zone at Mt Mucrone, Italy: mechanical and chemical behavior of allanite during mylonitization. *Lithos* **125**(1), 40–50.
- Chesner C. A. and Ettliger A. D. (1989) Composition of volcanic allanite from the Toba Tuffs, Sumatra, Indonesia. *Am. Mineral.* **74**(7–8), 750–758.
- Chew D. M., Sylvester P. J. and Tubrett M. N. (2011) U–Pb and Th–Pb dating of apatite by LA-ICPMS. *Chem. Geol.* **280**(1), 200–216.
- Cole D. R., Ohmoto H. and Lasaga A. C. (1983) Isotopic exchange in mineral-fluid systems. I. Theoretical evaluation of oxygen isotopic exchange accompanying surface reactions and diffusion. *Geochim. Cosmochim. Acta* **47**(10), 1681–1693.
- Compston W., Williams I. and Meyer C. (1984) U–Pb geochronology of zircons from lunar breccia 73217 using a sensitive high mass-resolution ion microprobe. *J. Geophys. Res.: Solid Earth* **89**(S02), B525–B534 (1978–2012).
- Copeland P., Parrish R. R. and Harrison T. M. (1988) Identification of inherited radiogenic Pb in monazite and its implications for U–Pb systematics. *Nature* **333**(6175), 760–763.

- Cox S. E., Farley K. A. and Hemming S. R. (2012) Insights into the age of the Mono Lake Excursion and magmatic crystal residence time from (U–Th)/He and ^{230}Th dating of volcanic allanite. *Earth Planet. Sci. Lett.* **319**, 178–184.
- Darling J. R., Storey C. D. and Engi M. (2012) Allanite U–Th–Pb geochronology by laser ablation ICPMS. *Chem. Geol.* **292**, 103–115.
- Dollase W. (1971) Refinement of the crystal structures of epidote, allanite and hancockite. *Am. Mineral.* **56**(3–4), 447–464.
- Dollase W. (1973) Mössbauer spectra and iron distribution in the epidote-group minerals*. *Z. Kristallogr.* **138**(1–4), 41–63.
- Duggan M. (1976) Primary allanite in vitrophyric rhyolites from the Tweed Shield Volcano, north-eastern New South Wales. *Mineral. Mag.* **40**, 652–653.
- Ercit T. S. (2002) The mess that is allanite. *Can. Mineral.* **40**(5), 1411–1419.
- Ewing R. C. (1999) Nuclear waste forms for actinides. *Proc. Nat. Acad. Sci.* **96**(7), 3432–3439.
- Ewing R. C., Haaker R. F. and Lutze W. (1982) Leachability of zircon as a function of alpha dose. In *Scientific Basis for Radioactive Waste Management*, vol. 5, pp. 389–397.
- Ewing R. C., Meldrum A., Wang L. M. and Wang S. X. (2000) Radiation-induced amorphization. *Rev. Mineral. Geochem.* **39**(1), 319–361.
- Exley R. (1980) Microprobe studies of REE-rich accessory minerals: implications for Skye granite petrogenesis and REE mobility in hydrothermal systems. *Earth Planet. Sci. Lett.* **48**(1), 97–110.
- Finger F., Broska I., Roberts M. P. and Schermaier A. (1998) Replacement of primary monazite by apatite-allanite-epidote coronas in an amphibolite facies granite gneiss from the eastern Alps. *Am. Mineral.* **83**, 248–258.
- Fitzsimons I., Kinny P., Wetherley S. and Hollingsworth D. (2005) Bulk chemical control on metamorphic monazite growth in pelitic schists and implications for U–Pb age data. *J. Metamorph. Geol.* **23**, 261–277.
- Gabudianu Radulescu I., Rubatto D., Gregory C. and Compagnoni R. (2009) The age of HP metamorphism in the Gran Paradiso Massif, Western Alps: a petrological and geochronological study of. *Lithos* **110**(1–4), 95–108.
- Geisler T., Pidgeon R., Van Bronswijk W. and Kurtz R. (2002) Transport of uranium, thorium, and lead in metamict zircon under low-temperature hydrothermal conditions. *Chem. Geol.* **191**(1), 141–154.
- Geisler T., Pidgeon R. T., Kurtz R., van Bronswijk W. and Schleicher H. (2003) Experimental hydrothermal alteration of partially metamict zircon. *Am. Mineral.* **88**(10), 1496–1513.
- Geisler T., Schaltegger U. and Tomaschek F. (2007) Re-equilibration of zircon in aqueous fluids and melts. *Elements* **3**(1), 43–50.
- Gieré R. (1986) Zirconolite, allanite and hoegbomite in a marble skarn from the Bergell contact aureole: implications for mobility of Ti, Zr and REE. *Contrib. Miner. Petrol.* **93**(4), 459–470.
- Gieré R. and Sorensen S. S. (2004) Allanite and other REE-rich epidote-group minerals. *Rev. Mineral. Geochem.* **56**(1), 431–493.
- Gindy A. (1961) Allanite from Wadi el Gemal area, eastern desert of Egypt, and its radioactivity. *Am. Mineral.* **46**, 985–993.
- Goldich S. and Mudrey Jr. M. (1972) Dilatancy model for discordant U–Pb zircon ages. In *Contributions to Recent Geochemistry and Analytical Chemistry*, pp. 415–418.
- Gregory C. J., Rubatto D., Allen C. M., Williams I. S., Hermann J. and Ireland T. (2007) Allanite micro-geochronology: a LA-ICP-MS and SHRIMP U–Th–Pb study. *Chem. Geol.* **245**(3–4), 162–182.
- Gregory C., Rubatto D., Hermann J., Berger A. and Engi M. (2012) Allanite behaviour during incipient melting in the southern Central Alps. *Geochim. Cosmochim. Acta* **84**, 433–458.
- Gromet L. and Silver L. T. (1983) Rare earth element distributions among minerals in a granodiorite and their petrogenetic implications. *Geochim. Cosmochim. Acta* **47**(5), 925–939.
- Guillong M. and Günther D. (2002) Effect of particle size distribution on ICP-induced elemental fractionation in laser ablation-inductively coupled plasma-mass spectrometry. *J. Anal. At. Spectrom.* **17**(8), 831–837.
- Gulson B. and Krogh T. (1973) Old lead components in the young Bergell Massif, south-east Swiss Alps. *Contrib. Miner. Petrol.* **40**(3), 239–252.
- Harlov D. E. and Hetherington C. J. (2010) Partial high-grade alteration of monazite using alkali-bearing fluids: experiment and nature. *Am. Mineral.* **95**(7), 1105–1108.
- Heaman L. and Parrish R. (1991) U–Pb geochronology of accessory minerals. In *Short Course Handbook on Applications of Radiogenic Isotope Systems To Problems in Geology*, vol. 19 (eds. L. Heaman and J. Ludden). Mineralogical Association of Canada, Toronto, pp. 59–102.
- Hermann J. (2002) Allanite: thorium and light rare earth element carrier in subducted crust. *Chem. Geol.* **192**(3–4), 289–306.
- Hetherington C. J. and Harlov D. E. (2008) Metasomatic thorite and uraninite inclusions in xenotime and monazite from granitic pegmatites, Hidra anorthosite massif, southwestern Norway: mechanics and fluid chemistry. *Am. Mineral.* **93**(5–6), 806–820.
- Hiess J., Condon D. J., McLean N. and Noble S. R. (2012) $^{238}\text{U}/^{235}\text{U}$ systematics in terrestrial uranium-bearing minerals. *Science* **335**(6076), 1610–1614.
- Hirata T. and Nesbitt R. W. (1995) U–Pb isotope geochronology of zircon: evaluation of the laser probe-inductively coupled plasma mass spectrometry technique. *Geochim. Cosmochim. Acta* **59**(12), 2491–2500.
- Hodges K., Parrish R. and Searle M. (1996) Tectonic evolution of the central Annapurna range, Nepalese Himalayas. *Tectonics* **15**(6), 1264–1291.
- Horn I., Rudnick R. L. and McDonough W. F. (2000) Precise elemental and isotope ratio determination by simultaneous solution nebulization and laser ablation-ICP-MS: application to U–Pb geochronology. *Chem. Geol.* **164**(3), 281–301.
- Horstwood M. S., Foster G. L., Parrish R. R., Noble S. R. and Nowell G. M. (2003) Common-Pb corrected in situ U–Pb accessory mineral geochronology by LA-MC-ICP-MS. *J. Anal. At. Spectrom.* **18**(8), 837–846.
- Ickert R. and Williams I. (2011) U–Pb zircon geochronology of Silurian-Devonian granites in southeastern Australia: implications for the timing of the Benambran Orogeny and the I–S dichotomy. *Aust. J. Earth Sci.* **58**(5), 501–516.
- Jackson S. E., Pearson N. J., Griffin W. L. and Belousova E. A. (2004) The application of laser ablation-inductively coupled plasma-mass spectrometry to in situ U–Pb zircon geochronology. *Chem. Geol.* **211**(1), 47–69.
- Janeczek J. and Eby R. (1993) Annealing of radiation damage in allanite and gadolinite. *Phys. Chem. Miner.* **19**(6), 343–356.
- Janots E., Negro F., Brunet F., Goffé B., Engi M. and Bouybaouène M. L. (2006) Evolution of the REE mineralogy in HP-LT metapelites of the Sebide complex, Rif, Morocco: monazite stability and geochronology. *Lithos* **87**(3), 214–234.
- Janots E., Brunet F., Goffé B., Poinssot C., Burchard M. and Cemic L. (2007) Thermochemistry of monazite-(La) and dissakisite-(La): implications for monazite and allanite stability in metapelites. *Contrib. Miner. Petrol.* **154**, 1–14.
- Janots E., Engi M., Berger A., Allaz J., Schwarz J. O. and Spandler C. (2008) Prograde metamorphic sequence of REE minerals in pelitic rocks of the Central Alps: implications for allanite-monazite-xenotime phase relations from 250 to 610°C. *J. Metamorph. Geol.* **26**(5), 509–526.

- Janots E., Engi M., Rubatto D., Berger A., Gregory C. and Rahn M. (2009) Metamorphic rates in collisional orogeny from in situ allanite and monazite dating. *Geology* **37**(1), 11.
- Janots E., Berger A., Gnos E., Whitehouse M., Lewin E. and Pettker T. (2012) Constraints on fluid evolution during metamorphism from U–Th–Pb systematics in Alpine hydrothermal monazite. *Chem. Geol.* **326–327**, 61–71.
- Kingsbury J. A., Miller C. F., Wooden J. L. and Harrison T. M. (1993) Monazite paragenesis and U–Pb systematics in rocks of the eastern Mojave Desert, California, USA: implications for thermochronometry. *Chem. Geol.* **110**, 147–167.
- Klimm K., Blundy J. D. and Green T. H. (2008) Trace element partitioning and accessory phase saturation during H₂O-saturated melting of basalt with implications for subduction zone chemical fluxes. *J. Petrol.* **49**, 523–553.
- Kohn M. J. and Malloy M. A. (2004) Formation of monazite via prograde metamorphic reactions among common silicates: implications for age determinations. *Geochim. Cosmochim. Acta* **68**, 101–113.
- Kohn M. J. and Vervoort J. D. (2008) U–Th–Pb dating of monazite by single-collector ICP-MS: pitfalls and potential. *Geochem. Geophys. Geosyst.* **9**(4).
- Kosterin A., Kizyura V. and Zuev V. (1961) Ratios of rare earth elements in allanites from some igneous rocks of northern Kirgiziya. *Geochemistry* **5**, 481–484.
- Krenn E., Harlov D. E., Finger F. and Wunder B. (2012) LREE-redistribution among fluorapatite, monazite, and allanite at high pressures and temperatures. *Am. Mineral.* **97**(11–12), 1881–1890.
- Levchenkov O. and Shukolyukov Y. A. (1970) A new method for calculating age and time of metamorphism of minerals and rocks without correction for ordinary lead. *Geochem. Internat.* **1**, 60–65.
- Ludwig K. R. (1998) On the treatment of concordant uranium–lead ages. *Geochim. Cosmochim. Acta* **62**(4), 665–676.
- Ludwig K. (2003a) *ISOPLOT 3.00: a geochronology toolkit for Microsoft Excel*. Berkeley Geochronological Center Special Publication, Berkeley.
- Ludwig K. (2003b) *Isoplot/Ex Version 3.00: a geological toolkit for Microsoft Excel*. Berkeley Geochronology Center Special Publication 4, 70 pp.
- Manzotti P., Rubatto D., Darling J., Zucali M., Cenki-Tok B. and Engi M. (2012) From Permo-Triassic lithospheric thinning to Jurassic rifting at the Adriatic margin: petrological and geochronological record in Valtournenche (Western Italian Alps). *Lithos*.
- Mezger K. and Krogstad E. (1997) Interpretation of discordant U–Pb zircon ages: an evaluation. *J. Metamorph. Geol.* **15**(1), 127–140.
- Miller C. F. and Mittlefehldt D. W. (1982) Depletion of light rare-earth elements in felsic magmas. *Geology* **10**(3), 129–133.
- Morrison C., Lambert D., Morrison R., Ahlers W. and Nicholls I. (1995) Laser ablation-inductively coupled plasma-mass spectrometry: an investigation of elemental responses and matrix effects in the analysis of geostandard materials. *Chem. Geol.* **119**(1), 13–29.
- Oberli F., Meier M., Berger A. and Rosenberg C. L. (2004) U–Th–Pb and ²³⁰Th/²³⁸U disequilibrium isotope systematics: precise accessory mineral chronology and melt evolution tracing in the Alpine Bergell intrusion. *Geochim. Cosmochim. Acta* **68**(11), 2543–2560.
- Oelkers E. H. and Poitrasson F. (2002) An experimental study of the dissolution stoichiometry and rates of a natural monazite as a function of temperature from 50 to 230 °C and pH from 1.5 to 10. *Chem. Geol.* **191**(1), 73–87.
- Palin R., Searle M., Waters D., Parrish R., Roberts N., Horstwood M., Yeh M. W., Chung S. L. and Anh T. (2013) A geochronological and petrological study of anatectic paragneiss and associated granite dykes from the Day Nui Con Voi metamorphic core complex, North Vietnam: constraints on the timing of metamorphism within the Red River shear zone. *J. Metamorph. Geol.* **31**(4), 359–387.
- Parrish R. R. (1990) U–Pb dating of monazite and its application to geological problems. *Can. J. Earth Sci.* **27**(11), 1431–1450.
- Parrish R. R., Gough S. J., Searle M. P. and Waters D. J. (2006) Plate velocity exhumation of ultrahigh-pressure eclogites in the Pakistan Himalaya. *Geology* **34**(11), 989–992.
- Petrík I., Broska I., Lipka J. and Šiman P. (1995) Granitoid allanite-(Ce): substitution relations, redox conditions and REE distributions (on an example of I-type granitoids, Western Carpathians, Slovakia). *Geol. Carpath.* **46**, 79–94.
- Pidgeon R., O’Neil J. R. and Silver L. T. (1966) Uranium and lead isotopic stability in a metamict zircon under experimental hydrothermal conditions. *Science* **154**(3756), 1538–1540.
- Poitrasson F. (2002) In situ investigations of allanite hydrothermal alteration: examples from calc-alkaline and anorogenic granites of Corsica (southeast France). *Contrib. Miner. Petrol.* **142**(4), 485–500.
- Rasmussen B., Muhling J. R., Fletcher I. R. and Wingate M. T. (2006) In situ SHRIMP U–Pb dating of monazite integrated with petrology and textures: does bulk composition control whether monazite forms in low-Ca pelitic rocks during amphibolite facies metamorphism? *Geochim. Cosmochim. Acta* **70**, 3040–3058.
- Romer R. L. and Siegesmund S. (2003) Why allanite may swindle about its true age. *Contrib. Miner. Petrol.* **146**(3), 297–307.
- Rubatto D., Regis D., Hermann J., Boston K., Engi M., Beltrando M. and McAlpine S. R. B. (2011) Yo-yo subduction recorded by accessory minerals in the Italian Western Alps. *Nat. Geosci.* **4**(5), 338–342.
- Saini H., Lal N. and Nagpaul K. (1975) Annealing studies of fission tracks in allanite. *Contrib. Miner. Petrol.* **52**, 143–145.
- Salje E., Chrosch J. and Ewing R. (1999) Is “metamictization” of zircon a phase transition? *Am. Mineral.* **84**(7–8), 1107–1116.
- Schärer U. (1984) The effect of initial ^{sup>230} Th disequilibrium on young UPb ages: the Makalu case, Himalaya. *Earth Planet. Sci. Lett.* **67**(2), 191–204.</sup>
- Schmitz M. D. and Schoene B. (2007) Derivation of isotope ratios, errors and error correlations for U–Pb geochronology using ²⁰⁵Pb–²³⁵U–(²³³U)-spiked isotope dilution thermal ionization mass spectrometric data. *Geochem. Geophys. Geosyst.* **8**(8), Q08006.
- Seydoux-Guillaume A. M., Paquette J. L., Wiedenbeck M., Montel J. M. and Heinrich W. (2002) Experimental resetting of the U–Th–Pb systems in monazite. *Chem. Geol.* **191**(1), 165–181.
- Silver L. T. and Deutsch S. (1963) Uranium–lead isotopic variations in zircons: a case study. *J. Geol.*, 721–758.
- Spear F. S. (2010) Monazite-allanite phase relations in metapelites. *Chem. Geol.* **279**, 55–62.
- Sláma J., Košler J., Condon D. J., Crowley J. L., Gerdes A., Hancher J. M., Horstwood M. S., Morris G. A., Nasdala L. and Norberg N. (2008) Plešovice zircon—a new natural reference material for U–Pb and Hf isotopic microanalysis. *Chem. Geol.* **249**(1), 1–35.
- Smith H. A. and Barreiro B. (1990) Monazite U–Pb dating of staurolite grade metamorphism in pelitic schists. *Contrib. Miner. Petrol.* **105**, 602–615.
- Smye A. J., Bickle M. J., Holland T. J. B., Parrish R. R. and Condon D. J. (2012) Rapid formation and exhumation of the youngest Alpine eclogites: a thermal conundrum to Barrovian metamorphism. *Earth Planet. Sci. Lett.* **306**(3–4), 193–204.

- Spandler C., Hermann J., Arculus R. and Mavrogenes J. (2003) Redistribution of trace elements during prograde metamorphism from lawsonite blueschist to eclogite facies; implications for deep subduction-zone processes. *Contrib. Miner. Petrol.* **146**, 205–222.
- Stacey J. S. and Kramers J. D. (1975) Approximation of terrestrial lead isotope evolution by a two-stage model. *Earth Planet. Sci. Lett.* **26**(2), 207–221.
- Steiger R. and DePaolo D. (1986) Genealogy of the basement of the Central Alps. *Terra Cognita* **6**(2), 127.
- Steiger R. and Jäger E. (1977) Subcommittee on geochronology: convention on the use of decay constants in geo- and cosmochronology. *Earth Planet. Sci. Lett.* **36**(3), 359–362.
- Storey C. D., Jeffries T. E. and Smith M. (2006) Common lead-corrected laser ablation ICP–MS U–Pb systematics and geochronology of titanite. *Chem. Geol.* **227**(1), 37–52.
- Tanner S. D., Cousins L. M. and Douglas D. (1994) Reduction of space charge effects using a three-aperture gas dynamic vacuum interface for inductively coupled plasma-mass spectrometry. *Appl. Spectrosc.* **48**(11), 1367–1372.
- Tomkins H. and Pattison D. (2007) Accessory phase petrogenesis in relation to major phase assemblages in pelites from the Nelson contact aureole, southern British Columbia. *J. Metamorph. Geol.* **25**, 401–421.
- Villa I. (2006) From nanometer to megameter: isotopes, atomic-scale processes, and continent-scale tectonic models. *Lithos* **87**(3), 155–173.
- Villa I. M. and von Blanckenburg F. (1991) A hornblende $Ar \pm Ar$ age traverse of the Bregaglia tonalite (SE Central Alps). *Schweiz. Mineral. Petrogr. Mitt.* **71**, 73–87.
- von Blanckenburg F. (1992) Combined high-precision chronometry and geochemical tracing using accessory minerals: applied to the Central-Alpine Bergell intrusion (central Europe). *Chem. Geol.* **100**(1–2), 19–40.
- Wasserburg G. (1963) Diffusion processes in lead–uranium systems. *J. Geophys. Res.* **68**, 4823.
- Weber W. J., Ewing R. C. and Wang L. M. (1994) The radiation-induced crystalline-to-amorphous transition in zircon. *J. Mater. Res.* **9**(03), 688–698.
- Wendt I. (1984) A three-dimensional U–Pb discordia plane to evaluate samples with common lead of unknown isotopic composition. *Chem. Geol.* **46**(1), 1–12.
- Wiedenbeck M., Alle P., Corfu F., Griffin W., Meier M., Oberli F., Quadt A., Roddick J. and Spiegel W. (1995) Three natural zircon standards for U–Th–Pb, Lu–Hf, trace element and REE analyses. *Geostand. Newslett.* **19**(1), 1–23.
- Williams I. S. (1998) U–Th–Pb geochronology by ion microprobe. In *Applications of Microanalytical Techniques to Understanding Mineralizing Processes* (eds. M. A. McKibben, W. C. Shanks, III and W. I. Ridley). *Rev. Econ. Geol.* pp. 1–35.
- Williams I., Tetley N., Compston W. and McDougall I. (1982) A comparison of K–Ar and Rb–Sr ages of rapidly cooled igneous rocks: two points in the Palaeozoic time scale re-evaluated. *J. Geol. Soc.* **139**(5), 557–568.
- Williams I., Compston W., Black L., Ireland T. and Foster J. (1984) Unsupported radiogenic Pb in zircon: a cause of anomalously high Pb–Pb, U–Pb and Th–Pb ages. *Contrib. Miner. Petrol.* **88**(4), 322–327.
- Williams M., Jercinovic M., Harlov D., Budzyń B. and Hetherington C. (2011) Resetting monazite ages during fluid-related alteration. *Chem. Geol.* **283**(3), 218–225.
- Wing B. A., Ferry J. M. and Harrison T. M. (2003) Prograde destruction and formation of monazite and allanite during contact and regional metamorphism of pelites: petrology and geochronology. *Contrib. Miner. Petrol.* **145**(2), 228–250.
- Zhang L. S. and Schärer U. (1996) Inherited Pb components in magmatic titanite and their consequence for the interpretation of U–Pb ages. *Earth Planet. Sci. Lett.* **138**(1), 57–65.

Associate editor: Trevor Ireland